Integrated EEG Acquisition System for MRI Electromagnetic Environment Applications

by

Tiantong Ren

A thesis submitted to the Graduate Faculty of
Auburn University
in partial fulfillment of the
requirements for the Degree of
Master of Science

Auburn, Alabama
August 1, 2015

Keywords: MRI, EEG, INA, Chopper stabilization

Approved by

Shumin Wang, Co-chair, Associate Professor of Electrical and Computer Engineering
Fa Foster Dai, Co-chair, Professor of Electrical & Computer Engineering
Goufu Niu, Alumni Professor of Electrical & Computer Engineering

Abstract

Nowadays, combined electroencephalography (EEG) and functional magnetic resonance imaging (fMRI) are used in neuroscience research since EEG have very high temporal resolution as compared to the Functional Magnetic Resonance Imaging (fMRI) which has very high spatial resolution but low temporal resolution. It shows great promise for helping researchers to develop a more comprehensive understanding of the neural behavior in human brain [1]. However, technological challenges of acquiring simultaneous fMRI/EEG signals arisen such as safety issues [2], effects of EEG on MRI acquisition, effects of MRI on EEG recording and other significant technical problems. The main purpose of this study is to evaluate effects of MRI induced electromagnetic fields on the EEG signal acquiring system and to design key module in MRI electromagnetic environment compatible EEG signal acquiring system for better signal quality.

Traditionally, EEG signals are acquired using contact electrodes together with connection leads to transit acquired biopotential signal out of scanner bore to preamplifier. In this work, from detail analysis on origins of artifacts which influences EEG signal quality and compared with traditional simultaneous MRI/EEG acquiring system [3], an in-bore MRI electromagnetic environment compatible EEG signal acquiring system on chip was proposed, with the key module: preamplifier implemented in 0.18um technology and simulated in Cadence. This thesis presents the design procedure and simulation results of the preamplifier. As result, an AC coupling chopper stabilized INA with second stage low pass filter is present. Simulation results shown it has desired differential gain and Common Mode Rejection Ratio (CMRR) ideal for

amplifying the weak biopotential while rejecting the stronger common mode interferers. Noise performance is greatly improved with the application of chopper stabilization technique which moves signal frequency band out of 1/f noise dominant frequency band before amplification.

Acknowledgments

First, I would like to thank my committee co-chairs, Dr. Shumin Wang and Dr. Fa Foster Dai who have been my advisors for master degree and for their expert guidance for me during the time I have spent at Auburn University.

I would also like to thank Dr. Niu who have graciously agreed to serve on my master's committee. His advises and support are very helpful and valuable. I also extend my gratitude to all the professors in the Electrical and Computer Engineering Department of Auburn University for all the help I have received.

In addition, I would like to thank all my fellow colleagues and associates Hai Lu, Yu Shao, Zhan Su, Dongyi Liao and Ruixing Wang. Thank you for your helps and constructive discussions. It has been a most delighting experience to work with them all together.

Finally, I want to acknowledge my parents, and all family members for their unconditional love and encouragement to keep me going forward throughout my pursuit of Master degree of Electrical Engineering.

Table of Contents

List of Tables

List of Figures

List of Abbreviations

AC   Alternating Current

ADC   Analog to Digital Conversion

CMRR   Common Mode Rejection Ratio

EEG   Electroencephalogram

MRI   Magnetic Resonance Imaging

NMR   Nuclear Magnetic Resonance

RF   Radio Frequency

SAR   Specific Absorption Rate

SNR   Signal-to-Noise Ratio

HBT   Heterojunction Bipolar Transistor

LNA   Low Noise Amplifier

SiGe   Silicon-Germanium

MHD   Magneto Hydrodynamic

EMF   Electromagnetic Field

MR   Magneto Resistance

GaAs   Gallium Arsenide

OPAMP   Operational Amplifier

SoC   System on Chip

Chapter 1 Introduction

1.1 Background and motivation

Electroencephalography (EEG) is a non-invasive method to record the spontaneous electrical activity of human brain. The first successful recording was made by German psychiatrist Hans Berger in 1924. Since then, EEG has been a key tool in studying human brain activity for over eight decades in extensive clinical and research uses, such as in epilepsy, sleep staging and psychophysiology.

MRI scanners use magnetic fields and radio waves to form images of the interested area in human. This noninvasive imaging property makes functional magnetic resonance imaging (fMRI) another widely used technique to investigate human brain function. It yields highly localized measures of brain activation, with a good spatial resolution but a low temporal resolution. EEG on the contrary has good temporal resolution to study the dynamics of brain function, but is poor in spatial resolution [6]. To provide the information necessary to understand the spatial-temporal aspects of information processing in the human brain, combined fMRI and EEG are applied in today's research in complementary to each other, making an effective way to examine the spatial and temporal dynamics of brain processes.

Unfortunately, due to interactions between the patient, EEG electrodes leads, and the magnetic fields in the scanner, EEG data collected in such experiments suffer from large artifacts which normally contains components in the EEG frequency range and are difficult to remove. Numerous hardware and software modifications were made in recent years to minimize artifacts

and improve simultaneous EEG and fMRI quality [5]. In all these systems, it seems to be the common way to transmit biopotential signals detected by electrodes out of the scanner room with connection leads. Advantage of this way is that all signal processing from pre-amplification to digitization can be done outside the scanner room in a more electromagnetic secure environment. However, connection leads related artifacts would heavily deteriorate signal quality and is hard to deal with even with modifications such as twisted pair leads and post signal processing. Considering this, improving signal quality by amplification and filtering before long connection leads transition is preferred.

In this thesis, main MRI electromagnetic fields and there influence on both tradition connection leads based EEG systems and in-bore EEG acquisition systems are compared. An in-bore MRI electronic environment compatible EEG acquisition system on chip is proposed.

1.2 Organization of the thesis

The thesis has been organized to discuss about the MRI electromagnetic environment influence on EEG acquiring systems and provides design architectures as well as techniques for a MRI electromagnetic environment compatible EEG acquiring SoC. Chapter 2 analyzes MRI electromagnetic environment and its influences on EEG recording in detail. Chapter 3 focus on MRI electromagnetic influences on in-bore EEG recording system, especially the performance of integrated circuit devices in strong static magnetic field. Chapter 4 describes the design of AC coupling chopper stabilized INA. Architectures, simulation of each building block are given with explanation. Chapter 5 draws conclusions and future work.

Chapter 2 Influence of MRI electromagnetic environment on EEG

2.1 MRI electromagnetic environment

Magnetic Resonance Imaging (MRI) is a medical imaging technique to investigate the anatomy and physiology of object's body. The principle of this technology is based on the use of a static magnetic field, gradient magnetic fields (spatial and temporal) and a radio frequency (RF) field. The latter is only present during the image acquisition phases, whereas the high intensity static field, obtained with a superconducting magnet, is emitted permanently. All these components creates a complex electromagnetic environment for testing object and devices [7].

2.1.1 Static magnetic field

MRI images are acquired from analysis of Nuclear magnetic resonance (NMR) signals which is used to selectively distinguish signals from certain atoms due to the magnetic behavior of their nuclei. Not all nuclei can be observed but only those which have spin and can be oriented within the magnetic field. This may be represented schematically as a small magnetized bar that can take up any orientation outside of a magnetic field. Suitable nuclei are certain isotopes such as hydrogen 1, carbon 13, phosphorous 31, nitrogen15, oxygen 17 and fluorine 19[4]. MRI uses the resonance of hydrogen, which is present in large quantities in human body. The nucleus of hydrogen contains a single proton, provided with a movement around an axis of rotation.

Object is placed in a very intense permanent static field (B_0), generated by superconducting coils cooled by liquid helium inside a first sealed enclosure, uniformly applied along the +Z-axis. The +Z-axis lies along the axis of the individuals body, extending from the feet through the

head in the center of the MRI machine. The XY plane, being perpendicular to the Z direction, describes the position within a particular slice across the subject being imaged.
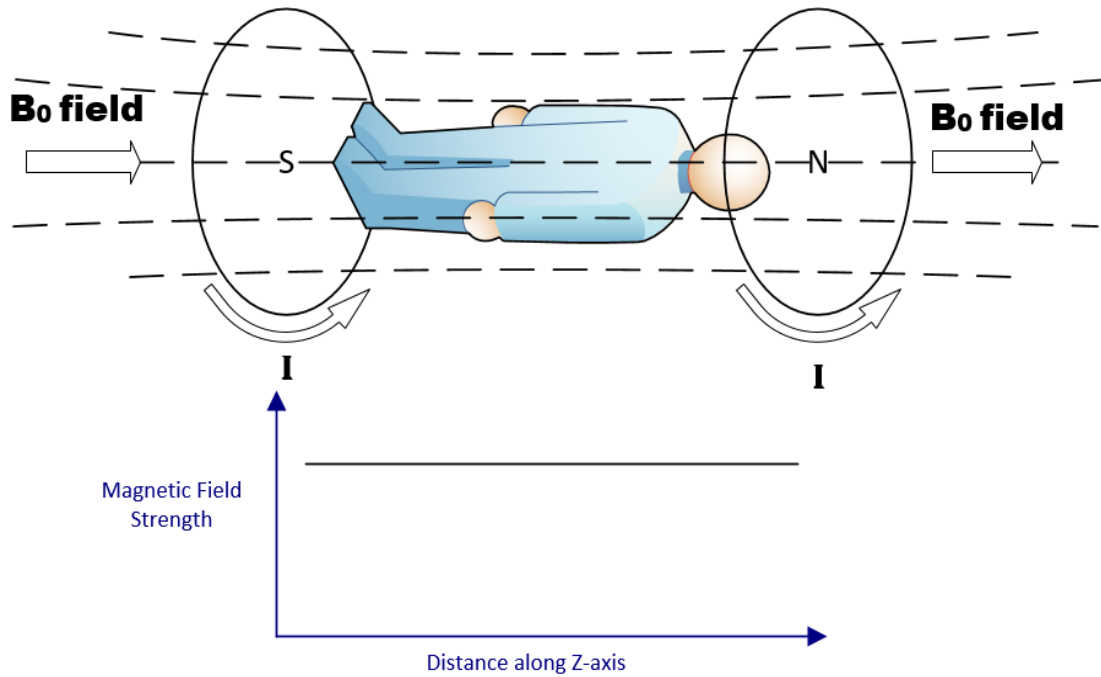
Fig. 2.1. Static (primary) magnetic field B0 in MRI scanner.

Hydrogen nuclei in the body placed into the magnetic field align along either the +Z-axis or the -Z-axis, thereby enabling MR imaging.

The most widely used magnets today in medical imaging centers are in 1.5 T, 3 T and7 T. Some 9 T or higher magnets are also being used for research purposes. With stronger static magnetic field being applied, more hydrogen nuclei inside object's body will subject to same direction. Thus, the image resolution would be increased and smaller volumes could be observed in detail.

2.1.2 Gradient magnetic field

The gradient magnetic field is used to localize the body slice to be measured. It contains three separate sets of gradient coils (x, y and z), each oriented perpendicular to others as shown in Fig below.
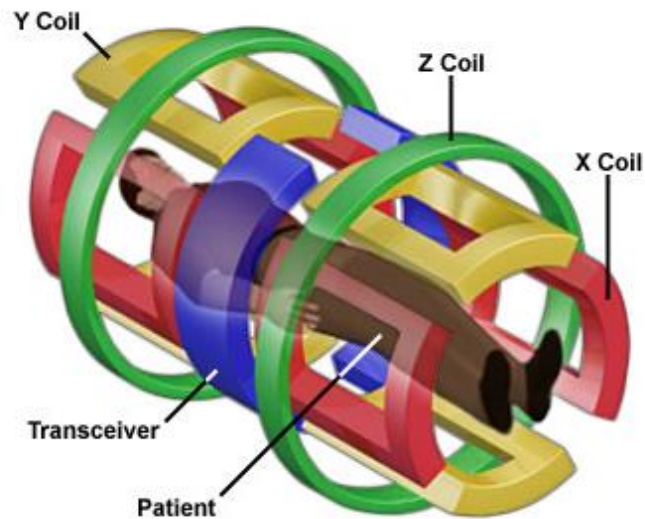
Fig. 2.2. MRI scanner gradient coils. [11]

The direction and magnitude of gradient fields can be appreciated by Ampère's Law and the right-hand rule. The Z-gradient magnetic field is produced using two coils carrying current in opposite directions as shown in Fig. 2.3. This is known as a Maxwell coil configuration. Maxwell coils produce a linearly increased field from magnet isocenter in both the +z and -z directions. When this is added to the constant (B_0) field, the result is a gradually increasing gradient along the z-axis. When this is added to the static magnetic field (B_0), the result is a gradually increasing gradient magnetic field along the z-axis. X and Y gradient is produced in the same way.
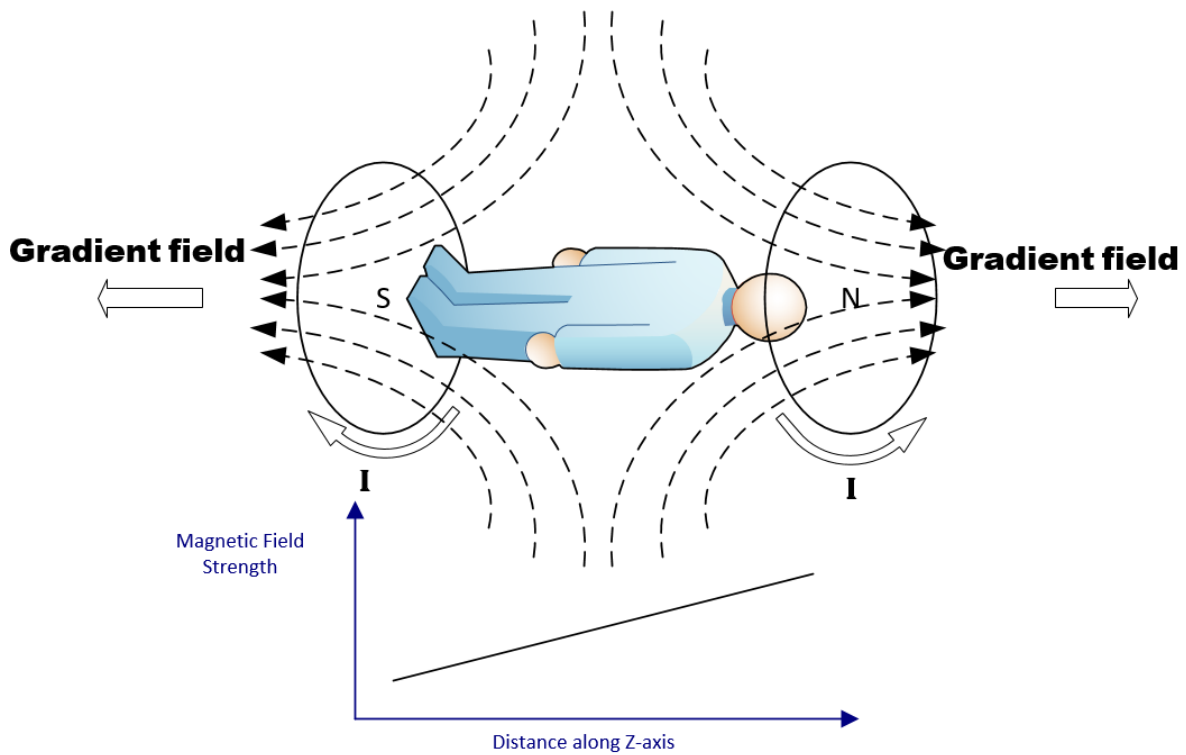
Fig. 2.3. Gradient magnetic field in MRI scanner.

These gradients are usually low frequency (up to 1 kHz) magnetic pulses with mostly trapezoidal waveforms. All of them are far less powerful than the main magnet but produce precise gradients in the three orthogonal directions. The gradients are used to create the spatial characteristics by producing the slices and voxels.

2.1.3 RF signal

The radio frequency (RF) system provides the communications link with the patient's body for the purpose of producing an image. The RF coils are located within the magnet bore and relatively close to the patient's body. These coils function as the antennae for both transmitting signals and receiving signals from the tissue. Different coils are used for different anatomical regions. The three basic types are body, head, and surface coils.
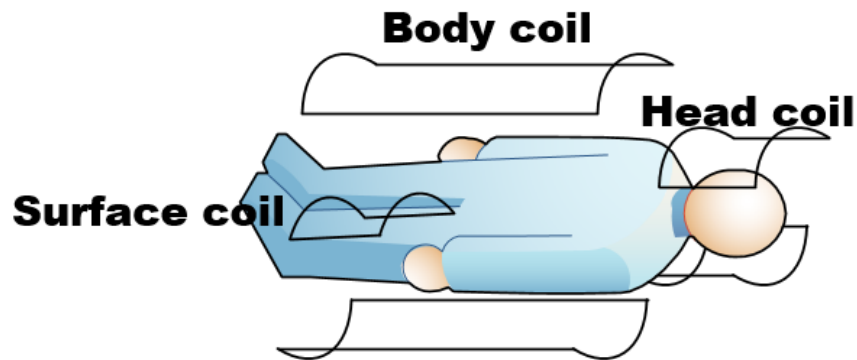
Fig. 2.4. Three types of RF coils (body, head, and surface) used for transmitting pulses and receiving signals.

The RF pulses excite protons and deflect the hydrogen-nuclei from their alignment. The return of the spins to their state of equilibrium in the static field forces the atom emits electromagnetic waves which contain a range of frequencies due to applied gradient magnetic field. The waves are then received by the antennas of the acquisition chain, and being processed in backend.

2.1.4 Summary

It would appear from the above description that three types of electromagnetic waves are used in MRI: I) high static magnetic field, which generates a net magnetization vector in the human body, for measurement of the proton density; II) gradient magnetic field (100 to 1,000 Hz), used to localize aligned protons inside the body, thus allowing spatial reconstruction of tissue sections into images; III) RF electromagnetic wave (10 to 400 MHz), which energizes the magnetization vector allowing its detection by the MRI scanner, converting tissue properties into MR images[5]. The spectrum of frequencies employed in MRI is summarized in Table. 2.1. Their influences on EEG will be discussed in detail.

Static magnetic field	Gradient magnetic field	Radiofrequency electromagnetic field
0 Hz	100–1,000 Hz	10–400 MHz

Table 2.1 Spectrum of frequencies used in MRI

2.2 EEG acquisition system

2.2.1 Basic of EEG recording system

In research and medical uses, most of the cerebral signal observed in the scalp EEG falls in the range of 0.1Hz–100Hz and its amplitude is below 100uV. EEG acquisition systems usually contains of electrodes for measuring, pre-amplifiers and filters for analog signal conditioning, analog to digital converters, and numeric processor or computer for further analysis.
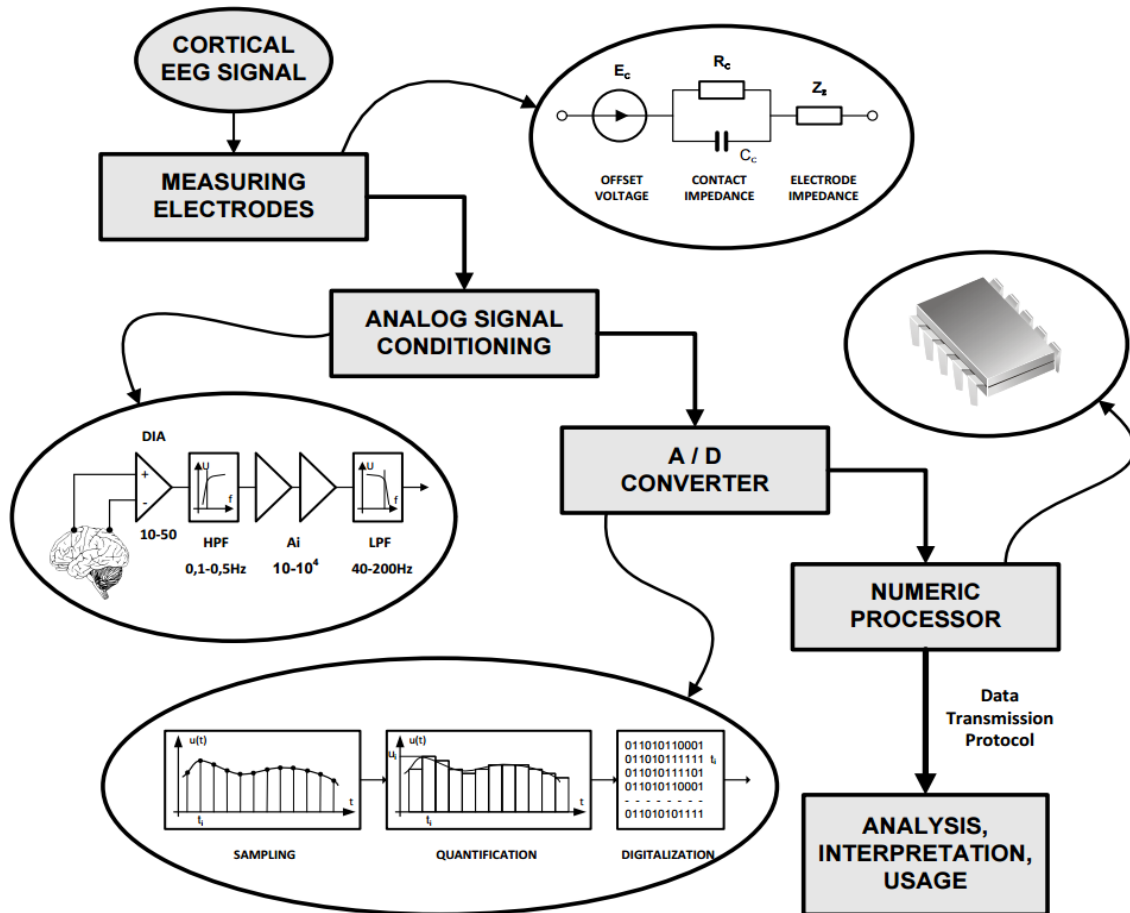
Fig. 2.5. Structure of EEG signal recording methodology [8]

2.2.2 Conventional MRI compatible EEG recording system

Electromagnetic fields in MRI scanner has influences on both signal quality and circuits reliability. The strong static and gradient magnetic field will add noise or even saturates components in electrical circuit. The presence of Lorenz force also excludes any ferromagnetic material components being used in MRI scanner. Meanwhile, the huge imaging artifacts caused by RF electromagnetic field during fMRI scanning can completely obscure the EEG signals. Therefore, for circumventing these problems and safety consideration [3], traditional simultaneous EEG/MRI recordings adopt special electrodes and leads connection based MRI compatible EEG acquisition system [9].
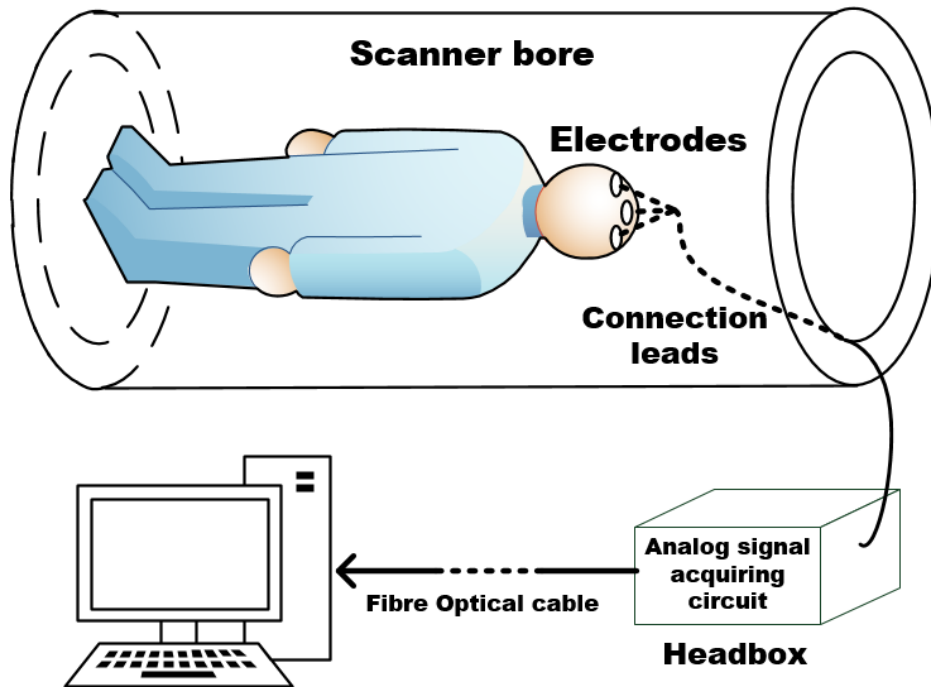
Fig. 2.6. Equipment schematic of MRI compatible EEG recording system

MRI compatible EEG recording systems with configuration as shown in Fig. 2.6 uses non-ferromagnetic electrodes such as silver chloride plated or gold-plated copper with silver wires, instead common paramagnetic materials. Long carbon fiber leads are used for connecting electrodes to a compact magnet-compatible local amplifier (headbox) outside the scanner with high resistance. These high resistance current limiting resistor fitted adjacent to each electrode as an essential part of our patient safety protocol for EEG recording in the MR scanner. In this way, all circuit components are moved out of the scanner room and thus facing much less electromagnetic field influences [10].

2.3 MRI electromagnetic effects on MRI compatible EEG recording system

Currently, degradation of EEG quality is a limiting factor for many applications of simultaneous EEG/fMRI recording. Beyond the main sources of noise (muscle artefact, eye movement, perspiration, mains interference etc.) already well known in common EEG recording, in simultaneous EEG/fMRI, electromotive forces can be induced in fixed conductor loops within rapidly changing gradient fields or RF electromagnetic fields as well as in moving conductor loops within the static magnetic field.

2.3.1 Pulse and movement artifact

Blood flow interact with high MRI static magnetic field (B_0) will induce electrical potentials due to Magneto hydrodynamic (MHD) effect, thus produce pulse artifacts which are widespread on the scalp[12]. Calculated values of flow potentials and current densities near the blood vessel compared with study of the effect of static magnetic field on blood flow rate shown that the MHD effect depends mainly on the strength of static magnetic field, magnetic permeability of blood, flow rate, and conductivities of fluid and vessel wall [13].
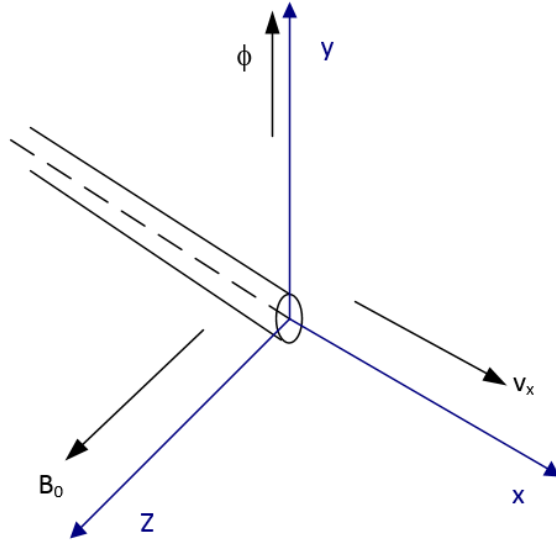
Fig. 2.7. Blood flow model with direction of applied static magnetic field (B_0), blood flow velocity (V_x), and induced electrical potential ⌀

The MHD related pulse artifact was largest in channels with frontal-polar or fronto-central electrodes. The amplitude of pulse artifact is directly related to B_0 and hence pulse artifact for scanners with higher B_0 will present a greater problem.

Meanwhile, Movement of the subject's head and electrode leads due to pulse, blood flow, talking or turning head also alters the area normal to the static field of a loop between electrode leads, giving an induced EMF in the leads. These induced EMFs will be amplified inside scanner and cause gross artifacts. As Faraday's law of electromagnetic induction stated, for a closed circuit within a magnetic field, voltage is induced in proportion to the rate of change in magnetic flux. This may be influenced by varying the magnitude of field, the size of the circuit, or its orientation relative to the field. Assuming electrode lead with length l is perpendicular to static magnetic field B0 and moving with speed vx as illustrated in fig. 2.8.

11
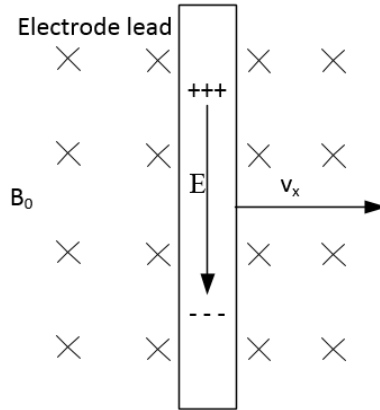
Fig. 2.8. Induced EMF of moving electrode lead in static magnetic field B0.

From Faraday's law:

$$EMF = \frac{B_0 \Delta A}{\Delta t} = B \frac{l \Delta x}{\Delta t} = Blv_x$$

It shows clearly that induced EMF of a moving electrode lead is proportional to both static magnetic field B0 and moving length of lead.

2.3.2 Image artifact

Image artifacts are due to the voltages induced by the time-varying magnetic fields (gradient magnetic field, RF pulses) applied during image acquisition. Induced large amplitude switching electromagnetic fields also applied on the electrode leads and the subject's head, significantly distort the EEG waveform. This can also be explained by Faraday's law of electromagnetic induction by seeing leads as loop conductors in a changing magnetic field.
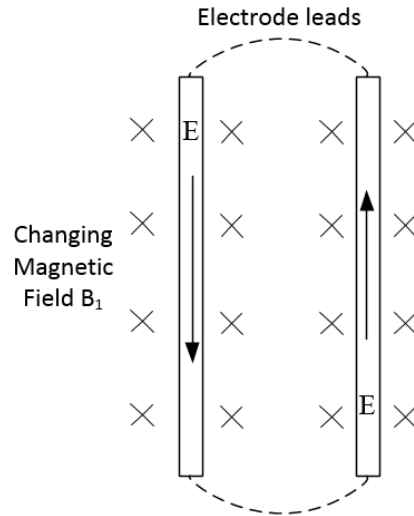
Fig. 2.9. Induced EMF of electrode lead in changing magnetic field.

As shown in figure 2.9. Assuming changing magnetic field is perpendicular to electrode leads (conductor loop) with length l and distance from each other is a. Induced EMF is produced in conductor in a changing magnetic field because the magnetic lines of force are applying a force on the free electrons in the leads and causing them to move.

From Faraday's law we have:

$$EMF = \frac{dB \bullet A}{dt} = \Delta Bla$$

There is still an obvious relationship between this induced EMF with frequency and field strength amplitude of the changing magnetic field as well as the electrode leads length.

2.3.3 Summary

From above discussion, it is clear that simultaneous MRI/EEG recording comes at premiums: using long leads to remove electronic system out of scanner bore and applying higher static magnetic field for better MRI image quality would incur a signal to noise penalty of EEG signal. It is exquisitely prone to motion-related artefacts and changing RF magnetic field due to both interelectrode leads and headbox connection leads, arising by virtue of Faraday's law.

Chapter 3 MRI electromagnetic environment influence on in-bore EEG recording system

For decays of modifying on signal quality of simultaneously MRI/EEG recording, many methods have been applied such as reducing the number and area lead loops, using interleaved MRI/EEG recording and complex back-end signal processing which improved EEG signal quality. Most of these techniques are based on complex backend digital processing and algorithm analysis.

Thinking from another prospective, the use of leads in conventional MRI compatible EEG recording system can be minimized even eliminated with analog signal conditioning circuits inside the scanner being close to the electrodes. In this way, EEG signal would be amplified before transition, thus becomes much more robust to electrodes and headbox connection leads related noise. The acquired signal could then be transit outside scanner room with fiber optical cable or even wireless communication with much less artifacts.
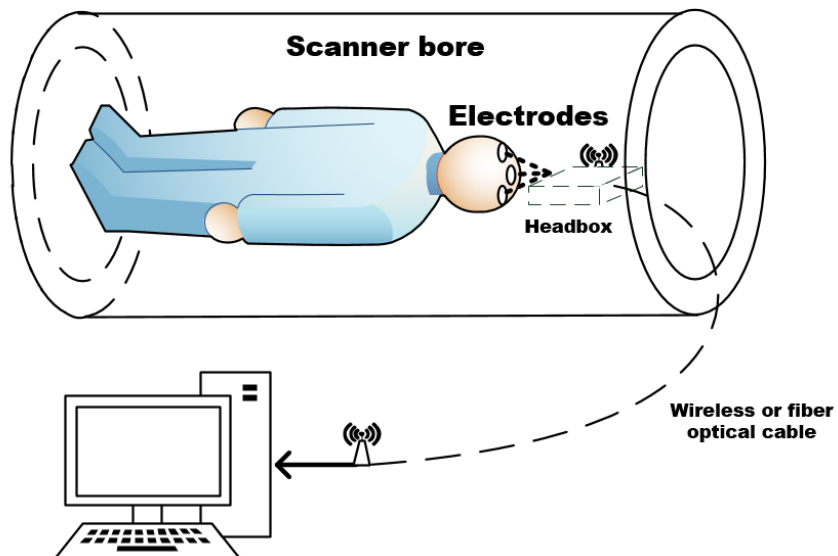
Fig. 3.1. Equipment schematic of proposed MRI compatible EEG recording system

However, MRI EMFs also have strong influences on performance of any electronic devises inside the scanner bore, and there are strict rules on materials being used inside scanner bore due to strong magnetic fields and patient safety consideration [15]. These are the very reason why traditional systems use connection leads to remove anything out of scanner bore except for electrodes which have to be inside. In this case, influences of MRI induced EMFs on integrated circuit devices in MRI electromagnetic environment shall be reviewed and compared to connection leads based systems.

Three main EMFs induced by MRI scanner as illustrated in Table. 2.1 are gradient magnetic field, RF signal and gradient magnetic field. Within them the influences of strong RF signal to nearby microelectronic system can be limited by certain EMC technics such as shielding. The gradient magnetic field is used for creating small amplitude difference of B_0 static magnetic field in space, so signals received by RF coil can be distinguished from different spatial coordinates, thus its influence is usually very small and can be neglect compared with B_0 field. This leaves the strong static magnetic field B_0 to be the major concern for any in-bore electronic system.

3.1 Static magnetic field influence on microelectronic devices

The biggest problem in MRI scanner for circuits function is the strong static magnetic field B_0 because of Hall Effect. The magnetic force on the moving charges will influences function of analog semiconductor devises in many ways such as variance in resistance, gain reduction and raised noise figure. Digital devises on the other hand are immune to such influences due to the fact that they only have two status: 0 or 1. All digital components from microprocessor to SD card are free to use in strong static magnetic field except for the magnetic media such as floppy disk or a hard drive as they would be easily erased.

16

3.1.1 Hall effect and magnetoresistance

The Hall effect is important in the analysis of semiconductor material. It results from the force on a charge moving in a magnetic field. Consider under the external electric field E_X, through the semiconductor sample flows a current I. Positive charges moving in the direction indicated by the vector v_X in the magnetic field B, the force would be in the direction $v_X \times B$.
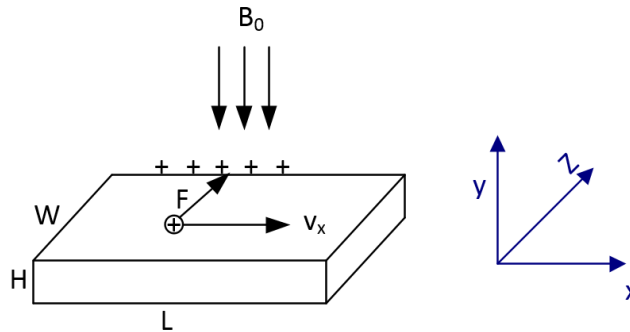
Fig. 3.2. Direction of the magnetic field B0, motion of the positive charge and Lorentz force.

The Hall bias is determined by the deviation of the charge carriers, which from a current through the conductor, under the action of the Lorenz force:

$$F = q(v_x \times B)$$

The force is in the z- direction. Thus the far face of the conductor becomes positively charged. On the other hand, if thinking current as negative charges moving in the negative -x direction, the force would be in the direction z-, so now the negative charges would be pushed toward the near face of the conductor and it would become negatively charged.
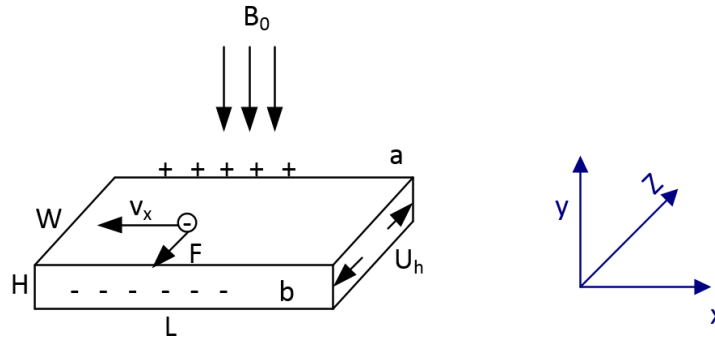
Fig. 3.3. Direction of the magnetic field B0, motion of the native charge and Lorentz force.

The potential difference U_h, called Hall bias, appears between its lateral faces, on the direction normal to both E and B:

$$U_h = V_a - V_b = \frac{IB_0}{neH}$$

Here n is mobile charges density and e is electron charge (1.602×10^{-19} coulombs).

Hall effect measurements is a useful technique for characterizing the electrical transport properties of metals and semiconductors. But in this situation that a complex semiconductor devices working in strong static magnetic field, it is really an annoying factor since it causes magnetoresistance and other problems which are discussed below.

Magnetoresistance is the property of a material to change its resistance in the presence of a magnetic field. The effect was first discovered by William Thomson in 1856. Magnetoresistance of a material consists of a physical component and a geometric component.

In a long Hall device (L >>W), Hall bias Uh compensates the Lorentz force on the carriers with the average velocity, vx. However the drift velocity of all the charge carriers is not same. The carriers moving with velocities less than vx are over compensated and those moving with velocities greater than vx are undercompensated, resulting in trajectories that are not along the applied electric field Ex. This results in an effective decrease of the mean free path and hence an increase in resistance of the semiconductor or metal. Now as the applied magnetic field is increased the trajectories of the charge carriers are more deviated which increases the magneto-resistance further.
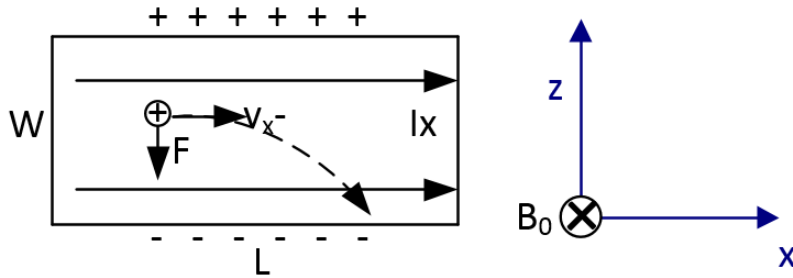
Fig. 3.4. Carriers moving with velocities less than vx and are over compensated.

In the short Hall plate (W>>L), the space charges generated by the Lorentz force on both sides are saturated due to injecting electrodes shorting them. The current density vectors are distorted in the majority area of the device. This distortion leads to a longer path length for current through the device under a transverse magnetic field. The corresponding increase in resistance in the presence of a magnetic field is called the geometric magneto-resistance (MR) effect [16].
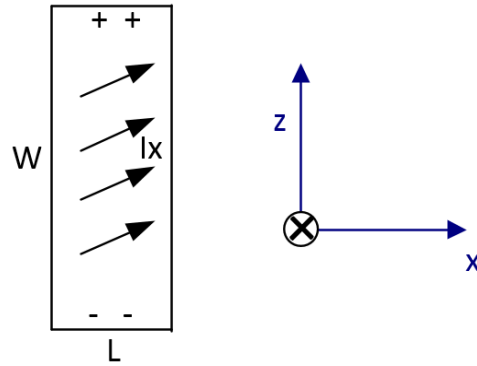
Fig. 3.5. Carriers moving through longer path in short Hall plate.

Device magnetoresistance value in applied static magnetic field is hard to calculate due to dependence on material properties such as mobility or carrier density, electrode configuration, material composition, shape of the device and more. Experiments and experiences shown that most non-ferromagnetic materials resistances increase no more than 5% in a strong orthogonal static magnetic field. For an integrated circuit, this will lead to variance in resistor value, transistor noise, Q factor of certain key elements and other.
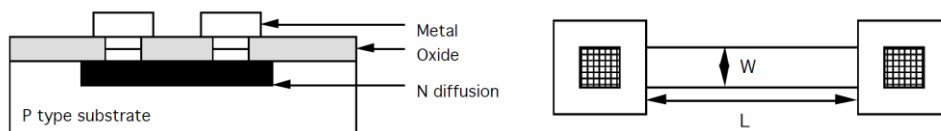
Fig. 3.6 diffused resistor (cross sectional and top view) [17].

3.2. Static magnetic field influence on transistors

3.2.1 Static magnetic field influence on BJT

From former experiences [18, 19, 20], when BJT is operating in the common emitter mode, its gain will be reduced by applying a strong magnetic field. This reduction is greatest when the magnetic field vector is perpendicular to the direction of minority carrier motion through the

base region. The degradation effect may be a result of several contributing factors such as magnetoresistance, a Hall biasing of the transistor junctions and a magnetic field dependent diffusion length.

If the magnetoresistance of transistor materials is treated as a field-dependent series resistance in the collector, base, and emitter, then the voltage applied across any two elements is divided not only by junctions but also voltage drop across the series resistance. As the magnetic field increases the fraction of the constant applied voltage biasing the junction decreases. Thus, the collector current would also decrease with magnetic field resulting in decrease in β. From discussion in magnetoresistance we can also see the change in diffusion length. This can be seen as an increase in the noise figure in transistor. The experiments results also shown that gain degradation and raised noise figure problems are more depend on the base width.

Nevertheless, Modern silicon–germanium (SiGe) bipolar transistors fabricated in IC chips are using better and better technology. BJT amplifiers as shown in Fig. 3.7 usually has small size vertical NPN sandwich structure (blue box in the figure) whose base width is determined by vertical distance between emitter diffusion and base diffusion, n+ buried layout is a low resistance contact to collector. In other words they are largely immune due to their very thin base.
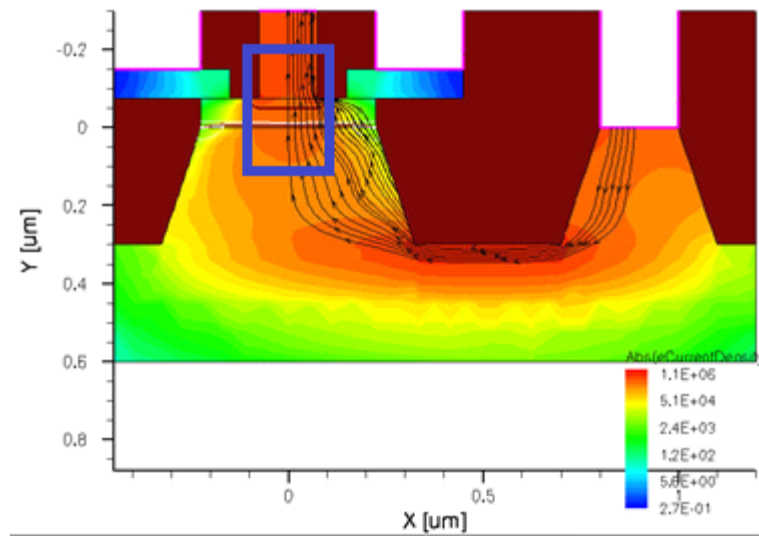
Fig. 3.7 Cross sectional view of SiGe bipolar transistors [21].

3.2.2 Static magnetic field influence on MOSFET

Compared to bipolar junction transistors, field-effect transistors are more sensitive to magnetic fields due to their high electron mobility and long, narrow channel. As shown in Fig. 3.8, an N-channel MOSFET working in a static magnetic field B_0. The Lorentz force induced Hall bias would be added directly on gate-substrate voltage reversely thus decrease its transconductance. Same result applies for P-channel MOSFET.
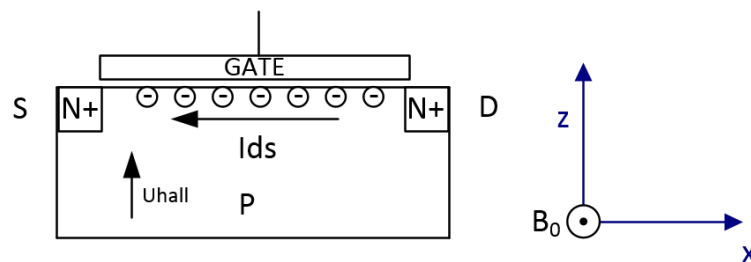
Fig. 3.8. Cross sectional view of N-channel MOSFET.

Here, the magnetic field is applied perpendicular to the current flow in the plane of the heterointerface. The Hall voltage modifies the effective gate-to-channel bias. This voltage is proportional to both the magnetic field B and the effective carrier velocity v and leads to the Hall electric field:

$$\Delta V_{gs} = U_h = vB_0(d + \Delta d)$$

Here v is the effective electron velocity, d is gate-to-channel distance and Δd is the effective thickness of electron sheet. It is explicit that the changed V_{gs} depends on the direction and strength of B_0.

The applied magnetic field will also influence the trajectories of the electrons between the source and drain of the MOSFET. The altered trajectories will also cause the transconductance gm to decrease which will lower the gain and increase the noise temperature of an amplifier.

3.3 Summary

Gain and noise figure of a semiconductor device are affected by magnetic field strength and orientation. This is a consequence of the Hall effect, which describes how the paths of motion of charge carriers within the semiconductor change as a result of the Lorentz force. These changes are detrimental to signal quality (SNR).

The degree of reduction was also related to the electron mobility of the semiconductor and geometry of device. Field-effect devices with long drain to source channel are easier to be infected by magnetic field than bipolar transistors. MOSFETs with lower mobility such as Si exhibit a lower sensitivity than those with high mobility such as GaAs. Conversely, SiGe devices

based on bipolar transistors have very thin base and hence they are much less sensitive to magnetic fields.

For operation in a strong static magnetic field as high as 7 T, there is no way to shield it using conventional ferromagnetic materials. The only way to reduce its influence is by geometrically setting the devises so that minimum charge motion is relatively perpendicular to the field. This means it is always better to orient the transistors that carrier flow in the bipolar transistors base region and field effect transistors drain source channel be parallel to the magnetic field. However the effect cannot be achieved in a single IC chip since BJTs are vertical structure transistors and MOSFETs are lateral structure transistors. When fabricated together, carrier flow in BJT base region is always perpendicular to those in MOSFET drain source channel. We can chose whole BJT or MOSFET design, or else, weigh the pros and cons of transistors in key components for the better result.

Therefore, with proper lay out and circuit design, MRI EMFs should theoretically have very little or no influence on in-bore integrated circuit. An in-bore MRI compatible EEG according system on chip is achievable and would reduce the use of connection leads.

Chapter 4 MRI compatible EEG acquisition system design

So based on the thorough analysis of MRI electromagnetic environment influences on EEG on both system and circuit level, the possibility of an in-bore MRI compatible EEG acquiring system is valid with orientation specific layout of semiconductors and proper shielding. Therefore, an MRI compatible wireless EEG acquiring system is proposed as illustrated in Fig. 4.1.
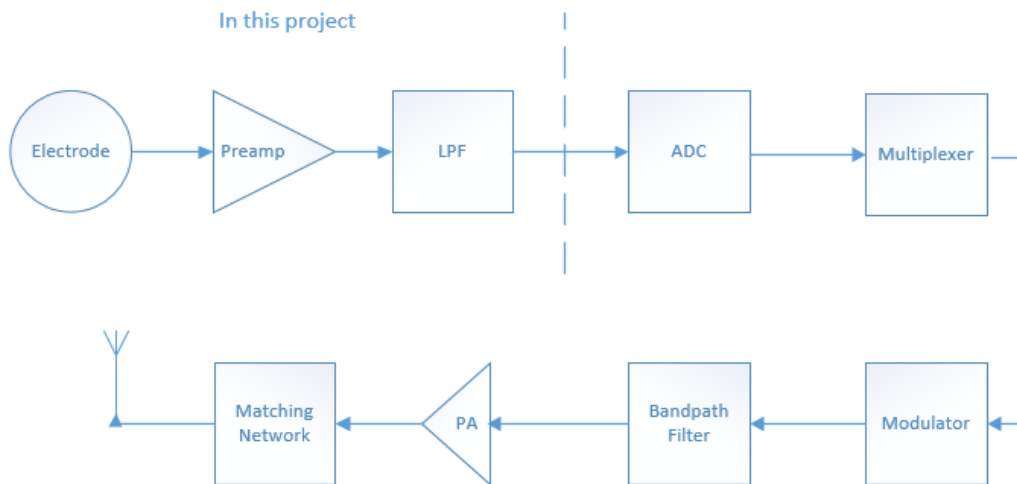
Fig. 4.1. Proposed wireless EGG acquiring system structure.

A basic wireless EEG system includes EEG preamplifier, low-pass filter, analog to digital converter, wireless transmitter, wireless receiver and processing, display unit. The collected EEG signals are sent to preamplifier through measuring electrodes, and the amplified output signal of preamplifier passes through a low-pass filter, then transmitted after analog to digital conversion (ADC) by wireless transmitter.

In this thesis, we concentrate more on signal acquisition, amplification and filtering. Further process such as digitization, channel multiplexing and signal transmitting are not discussed in

this project since analog signal to noise ratio (SNR) up to here (before digitization) dominants entire system signal quality.

Discussion and analysis are done on concerned parts includes electrodes that are used to acquire voltage signal from scalp and twisted pair leads used to connect these measuring electrodes to analog signal precession system on chip. Chip front end contains AC coupling chopper stabilized instrumentation amplifier and low pass filter.

4.1 Measuring electrodes and connection leads

4.1.1 Measuring electrodes

The internationally standardized 10-20 system is employed to record the spontaneous EEG. In this system 21 electrodes are located on the surface of the scalp, as shown in Fig.4.1. The positions are determined as follows: Reference points are nasion, which is the delve at the top of the nose, level with the eyes; and inion, which is the bony lump at the base of the skull on the midline at the back of the head. From these points, the skull perimeters are measured in the transverse and median planes. Electrode locations are determined by dividing these perimeters into 10% and 20% intervals. Three other electrodes are placed on each side equidistant from the neighboring points [22].
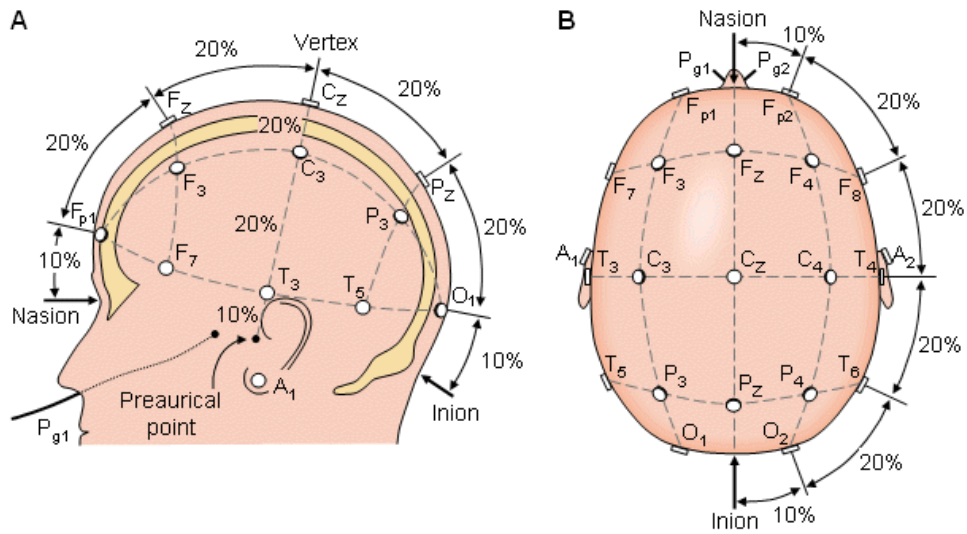
Fig. 4.1. The international 10-20 system seen from (A) left and (B) above the head [22]

Bipolar or unipolar electrodes can be used in the EEG measurement. In the first method the potential difference between a pair of electrodes is measured. In the latter method the potential of each electrode is compared either to a neutral electrode or to the average of all electrodes.
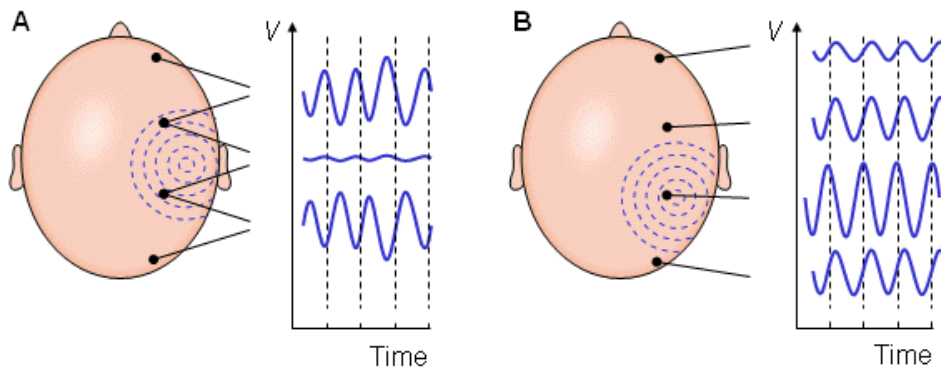
Fig. 4.2. (a) Bipolar and (b) unipolar measurements [22].

In this project, we analysis the system for 1 channel signal acquisition which can be used for both bipolar and unipolar method. Only non-ferromagnetic electrodes are used due to the

presence of strong static magnetic field. A hazard which must be assessed is the heating due to eddy currents induced in electrodes placed in a time-varying magnetic field. Experiment results shown that heating of an AgIAgC1 electrodes due to eddy currents is minimal [24].

4.1.2 Connection leads

Electrodes are connected to system board and other electrodes by connection leads. With the in bore system broad put right beside object's head, the length of connection leads are dramatically decreased. From above discussion we know that by reducing the area and total length of interelectrode lead loops should reduce the PA due to lead movement and RF induced artifacts.

As a general rule, it is advised to twist electrode leads together from the subjects head to the amplifier inputs. This configuration leaves only small loops at the head in which current can be induced. Because currents induced in consecutive twists by motion and gradient switching cancel each other since the currents flow in opposing directions.
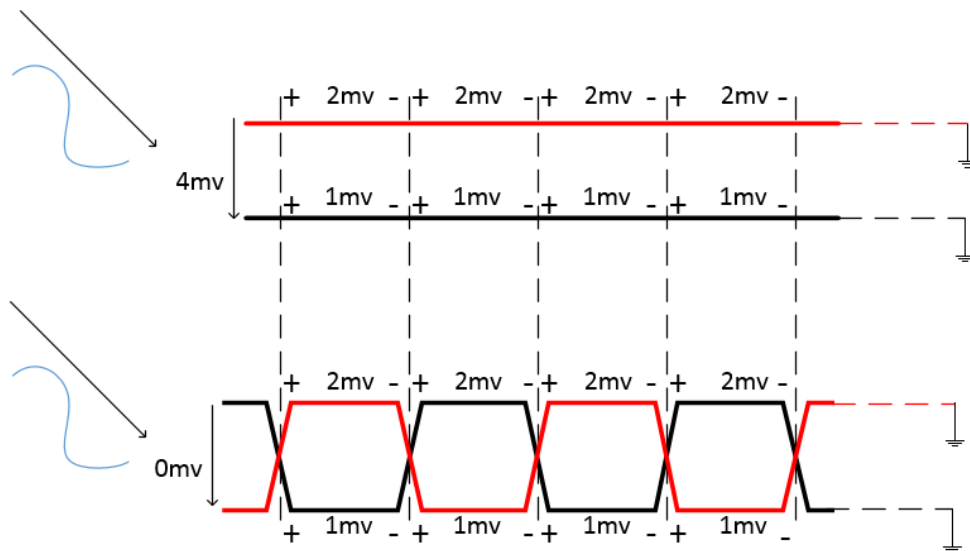
Fig. 4.3. Induced field in parallel pair leads and twisted pair leads

28

As shown in Fig.4.3. Noises are generated in signal lines by magnetic fields from the environment. In parallel pair, the interference to the red wire generate more induced voltage per unit length compared to those in black wire. Total difference at the destination is 4mV. While in the twisted pair case, total difference is 0V at destination because twists wires alternatively subjected to same level of interference and thereby total difference at destination is 0V. This phenomenon is simulated in CADFEKO suite 7.0 for detail.

A "bird cage" head coil used in 3T scanner is modeled as shown in Fig. 4.4. The transit RF signal (B_1 field) frequency is 123.3 MHz and amplitude is 1V.
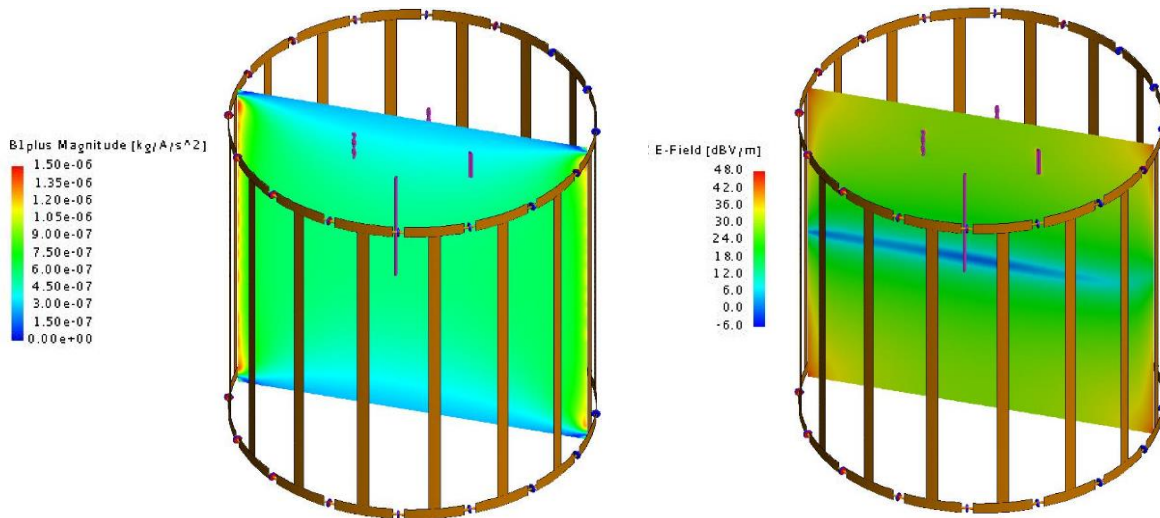
Fig. 4.4. Modeled "bird cage" head coil with B1 field and E field

Connection leads were modeled in form of twisted and non-twisted pairs and the reference group pairs are in different length. Since the E- field are uniformly distributed in coaxial direction and is symmetric along the center phase, 2 sets of connection leads were simulated in "bird cage" coil induced field, one in lateral direction and another one in horizontal direction. As should in Fig. 4.5, four pairs of connection leads are either 10 cm or 2.5 cm in length.

(a) In lateral direction

(b) In horizontal direction
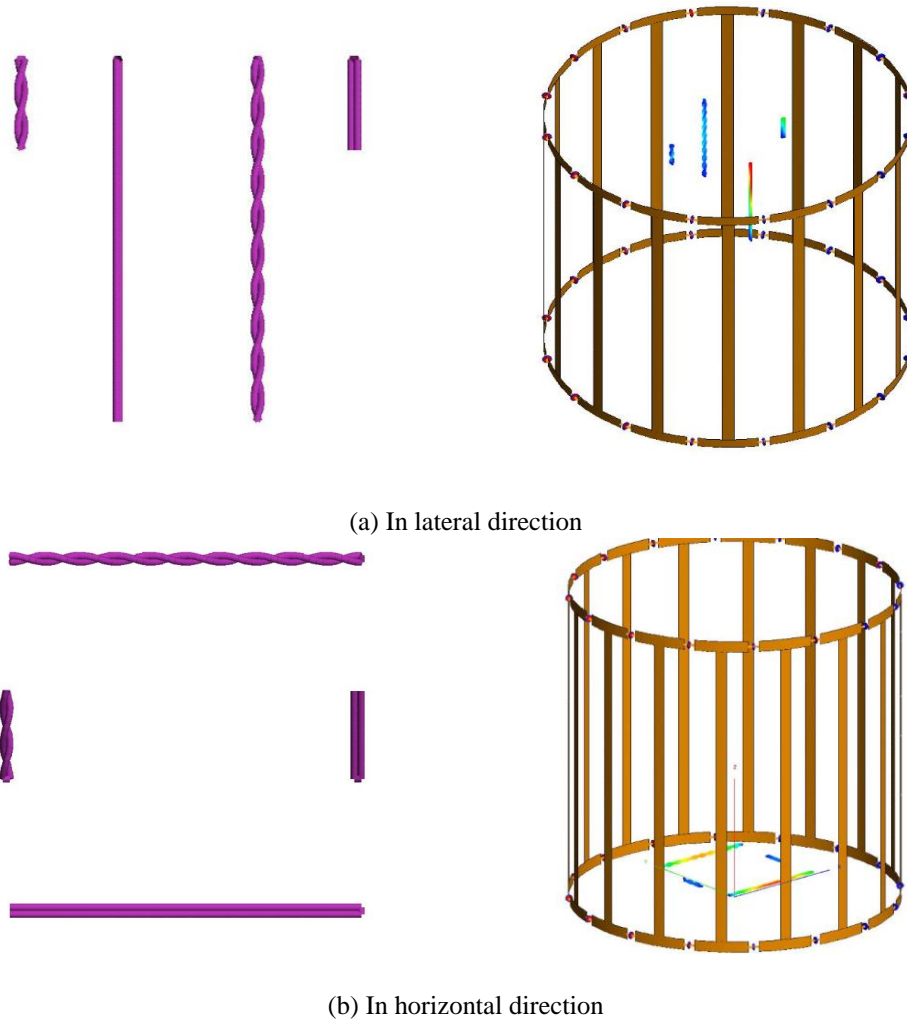
Fig. 4.5. Modeled connection leads in "bird cage" head coil in (a) lateral direction and (b) horizontal direction

As simulation result shown in Fig. 4.6, induced current in twist pairs are much smaller than in non-twist pairs, and is dramatically decreased with shorter length. This result is consistent with our assumption and is in support of the idea that shorter length of twisted pair would lead to much less noise and interface.
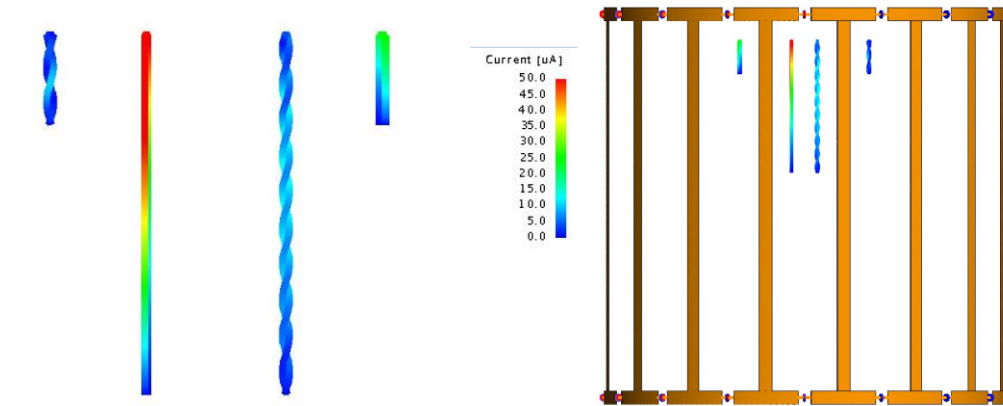
(a) Lateral direction
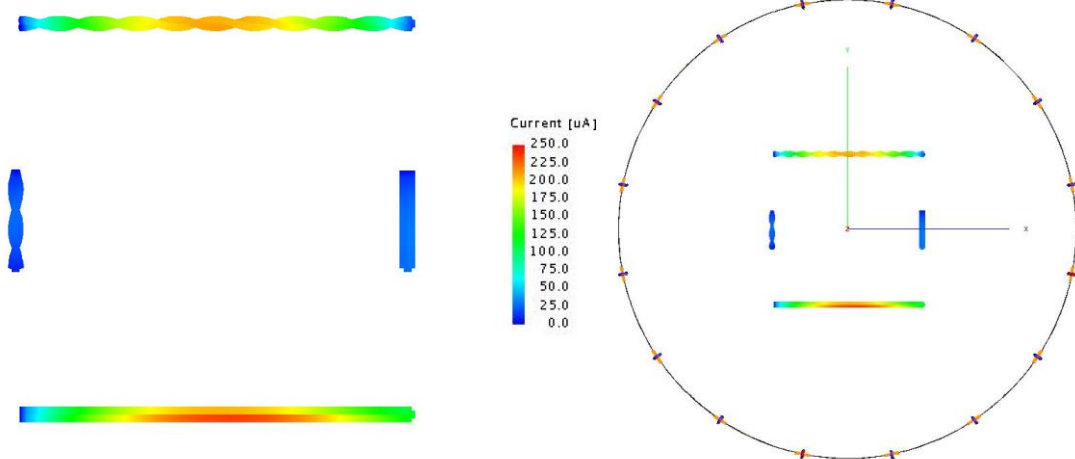
(b) Horizontal direction

Fig. 4.6. Simulation result of induced currents in connection leads of (a) lateral direction and (b) horizontal direction

Another safety consideration is that large voltages can be induced in loops formed by EEG wire resulting from the RF pulses witch would cause danger to object. This was identified as the single most important risk factor in EEG/fMRI. Current-limiting resistors are usually adopted to ensuring patient safety. These current-limiting resistors should be placed as near as possible to the EEG electrodes. Their value is determined based on the ratio of the EMF induced voltage to maximum allowable current, which is proportional to the square root of the whole-body specific absorption rate (SAR) [3].

4.2. Preamplifier requirements and architecture

First stage of analog signal acquiring system is critical to signal quality in later process. From analyzing of the low frequency low amplitude EEG signal and the environment influences to signal, input output signal parameters and listed for design of first stage preamplifier. Noise and artifact components are also considered for better performance. In the end, a low noise chopper stabilized high CMRR differential amplifier is designed and compared with common low noise amplifier and differential amplifier.

4.2.1 Preamplifier input signal and desired output signal

From electrodes and connection leads we can get brain signals which different frequency bands relate to various brain states. They are categorized into five basic groups named Delta, theta, alpha, beta and gamma as listed in table 4.1.

EEG band	Frequency range	Mental states and conditions
Delta	0.1Hz to 3Hz	Deep, dreamless sleep, unconscious
Theta	4Hz to 7Hz	Intuitive, creative, recall, imaginary, dream
Alpha	8Hz to 12Hz	Relaxed, tranquil, conscious
Low Beta	12Hz to 15Hz	Formerly SMR, relaxed yet focused, integrated
Midrange Beta	16Hz to 20Hz	Thinking
High Beta	21Hz to 30Hz	Alertness, agitation
Gamma	30Hz to 100Hz	Higher mental activity

Table. 4.1. EEG frequency bands and related brain states

The amplitude of an EEG signal measured on the scalp ranges typically from 10 uV to 100 uV in a normal adult. So for the output signal range of first stage amplifier to be from 10mV to 100mV, the desired differential gain should be larger than 1000 (60dB).

As we discussed above, EEG is differential signal from two electrodes, so it always comes with big common-mode interference from the mains correlate the biopotential signals. Besides, skin-electrode interface would generate offset voltage which may differ from each other in static magnetic field. Former measurements reveal that the offset of the AgCl electrodes can reach up to 50 mV depending on the preparation of the skin and the contact between the electrodes and the tissue [25]. This indicates that the amplifier should have high common mode reject ratio. We know the desired differential gain is 1000 (60dB), so if we want to decrease offset voltages to a negligible level (say below 0.5mV), the first stage amplifier should have a minimum CMRR:

$$CMRR = 20\log(\frac{1000}{\frac{0.5mV}{50mV}}) = 100dB$$

Another critical problem for EEG signal acquisition is its extreme low frequency range. As shown in Table. 4.1, desired EEG frequency band range from 0.1Hz to 100Hz in which the noise is dominated by 1/f noise. Distinguishing 10 uV signal from noise of 500nV/(sqrt(Hz)) would be hard. Thus for acquiring such low amplitude signal, modifications must be done for acceptable signal to noise ratio.

Frequency range	0.1Hz to 100Hz
Voltage amplitude	10uV to100uV
Common-mode interface	Below 100mV
DC offset	30mV to 100mV
Input signal type	Differential with common ground

(a) Preamp input signal

Differential gain	60dB
CMRR	> 100dB
Effective bandwidth	0.1Hz to 100Hz
Input impedance	>50M Ω

(b) Desired preamplifier parameters

Table. 4.2. Input signal value and desired amplifier parameters

In conclusion, preamplifier input signal and desired amplifier parameters are given in table. 4.2. According to system requirement, a high gain preamplifier with low noise and high common mode rejection ratio is needed. We design this preamplifier first by comparing commonly used differential amplifier structures.

4.2.2 Difference amplifier

Operation amplifiers are most commonly used as difference amplifiers due to their input configuration. By connecting one voltage signal onto one input terminal and another voltage signal onto the other input terminal the resultant output voltage will be proportional to the difference between the two input voltage signals of IN+ and IN-. This structure is also known as subtractor. Its configuration is shown below:
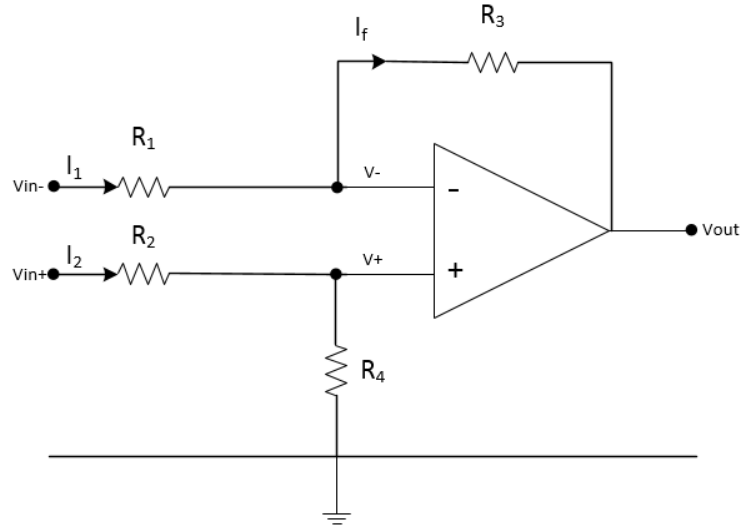
Fig. 4.7. Schematic of differential amplifier

Then the transfer function for a Difference Amplifier circuit is given as:

$$I_1 = \frac{V_{in-} - V_-}{R_1}, I_2 = \frac{V_{in+} - V_+}{R_2}, I_f = \frac{V_- - V_{out}}{R_3}$$

Here
$$V_- = V_+$$

$$V_+ = V_{in+}(\frac{R_4}{R_2 + R_4})$$

If V_{in+}=0, then
$$V_{out(-)} = -V_{in-}(\frac{R_3}{R_1})$$

If V_{in-}=0, then
$$V_{out(+)} = V_{in+}(\frac{R_4}{R_2 + R_4})(\frac{R_1 + R_3}{R_1})$$

$$V_{out} = V_{out(-)} + V_{out(+)}$$

When R1 = R2 and R3 = R4, the above transfer function can be simplified to:

$$V_{out} = (V_{in+} - V_{in-})\frac{R_3}{R_1}$$

Major limitations of this type of amplifier design however, make it impossible for EEG acquisition.

First, consider input impedance. Difference amplifier input impedance is relatively low, as determined by the values of the resistors, which may be in the order of 100 kΩ. Each input voltage source has to drive current through an input resistance, which has less overall impedance than that of the op-amps input alone. This may be OK for a low impedance source such as the bridge circuit above, but not so good for a high impedance source as EEG electrode (usually higher than 5k Ω).

Second, the resistors in each leg needs to be matched. Difference in input impedances results a difference current would flow through each leg, causing the CMR to suffer. The level of matching within the resistor pairs, not the op amp itself, predominately determines its CMR, which can be calculated as [26]:

$$CMRR = 20\log(\frac{1+\frac{R_2}{R_1}}{R_{mismatch}})$$

$R_{mismatch}$ = total mismatch of the resistor pairs in fractional form. For example, assume R1 = R2 = R3 = R4 (providing unity gain), and the resistor mismatch is 1%. Using the above equation:

CMRR = 20 log (200) = 46 dB

Even when resistors are perfectly matched, fluctuations due to temperature, as any difference in temperature coefficients among the resistors will further increase the mismatch and result in worse CMR. Accounting for all of these factors and limitations, an instrumentation amplifier (INA) is usually the best solution for relatively high-performance applications.

4.2.3 Instrumentation amplifier

Instrumentation amplifier (INA) is a specialized amplifier, most commonly used in measurement systems. INAs and operational amplifiers (OPAMPs) are based on the same basic building blocks, it can be seen as difference amplifiers added with input buffers. As mentioned above, difference amplifiers using OP AMPs with feedback loops has finite impedance which would load the input signals. Also, any mismatch in input impedances would degrade CMR so common mode is still present at the output and limits the dynamic range of the output.

INAs are specifically designed for their differential-gain and common-mode-rejection (CMR) capabilities. Two common circuits are utilized to create an INA, one based on two amplifiers and one based on three amplifiers.

4.2.3.1 Two-Op-Amp INA

This INA circuit is based on two OPAMPs shown as Fig. 4.8. The two-op-amp INA input signals feed directly into the input pins of the OPAMPs, which generally have impedances in the millions of ohms. Amplifier overall gain is set via one resistor R_G [27]:

$$Vout = (V_{IN+} - V_{IN-})(1 + \frac{R_2}{R_1} + \frac{2R_2}{R_G})$$
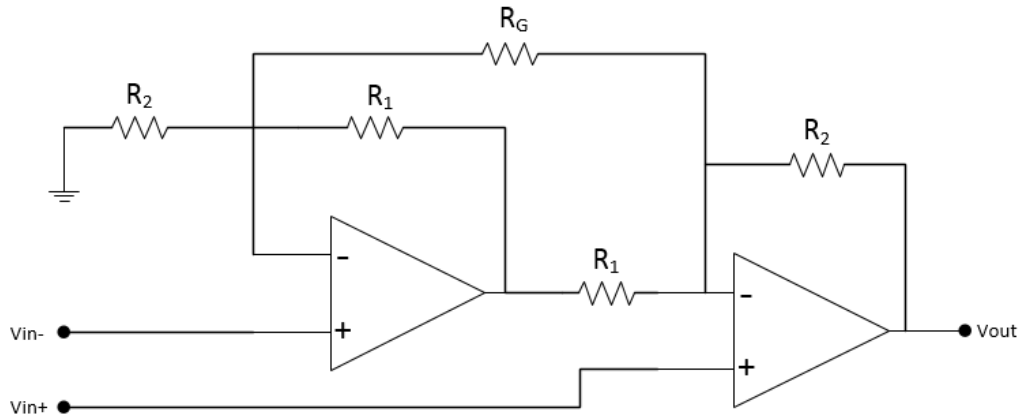
Fig. 4.8. Schematic of a Two-Op-Amp INA

A problem of this circuit is that the second OPAMP amplifies the input signal at the non-inverting node by 1 + R1/R2. Thus, if the common mode of the input signal is too high, the amplifier will be saturated due to headroom limit.

Another problem is that due to the difference in the input signal paths, there is a delay difference between the differential input signals, which degrades CMR across frequency. And similar to the difference-amplifier circuit, the matching of the resistor ratios still limits the CMR at dc.

A monolithic INA based on this two-op-amp architecture will inherently have better resistor matching and temperature tracking, relative to a discrete solution, as silicon-based resistors can be trimmed to provide matching on the order of 0.01%. Still, the two-op-amp INA architecture has some definite limitations that cannot be overcome without changing the architecture of the circuit.

4.2.3.2 Three-Op-Amp INA

This INA circuit is based on three OPAMPs as in Fig.4.9. It can be seen as a difference amplifier (OPAMP 3) with two OPAMP input buffers (OPAMP1 and 2).
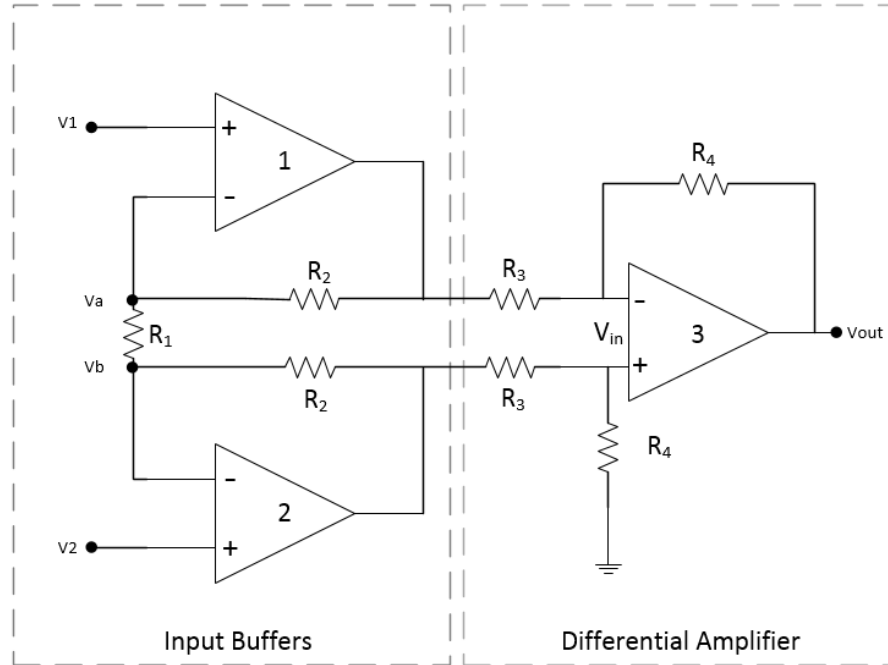
Fig. 4.9. Schematic of a Three-Op-Amp INA

Two non-inverting amplifiers acting as buffer amplifiers with a gain of $1 + 2R2/R1$ for differential input signals and unity gain for common mode input signals. And here we have:

$$V_1 = V_a, V_2 = V_b$$

Voltage drop across resistor is
$$V_{dm} = V_a - V_b$$

Differential gain of the circuit can be varied by changing the value of R1:

$$Vout = (V_2 - V_1)(1 + \frac{2R_2}{R_1})(\frac{R_4}{R_3})$$

$$A_{dm} = (1 + \frac{2R_2}{R_1})(\frac{R_4}{R_3})$$

When common-mode voltage is applied to the amplifiers inputs, the voltages on each side of R1 will be equal, and no current will flow through this resistor. Since no current flows through R1, common-mode signals are only passed through the first two amplifiers at unity gain. The common mode gain of the instrumentation amplifier is:

$$A_{cm} = \frac{R_4}{R_3} \frac{1}{CMRR_3}$$

CMRR3 is the common mode rejection ratio of second stage amplifier (OPAMP3). So the total common rejection ratio (CMRR) in decibels can be calculated by:

$$CMRR = 20 \log(1 + 2\frac{R_2}{R_1}) + CMRR_3$$

Similar to the previous architectures that have been discussed, the CMR performance depends on the resistor ratio matching:

$$CMRR = 20 \log (gain/Rt)$$

In three OPAMP INA configuration, high and well-matched impedances are easier to achieve, alleviating one of the main concerns with the simple differential circuit. It also accommodate a wide common-mode range (limited by the headroom of the first two amplifiers), regardless of the gain.

4.3 Design of three OPAMP instrumental amplifier

From above discussion we can see that three OPAMP instrumental amplifier is the idea structure for preamplifier since it not only provides high CMRR and high input impedance, the 2 amplification stage can also give enough gain. An INA prototype was then design and

implemented in 0.18um SiGe (BCS180G) technology and simulated in cadence. Design procedure and simulation results are discussed below.

4.3.1 OPAMP design

Operational amplifier cell is the key element in this design. Topology used here is an adaptation of the work in [28]. This topology is chosen mainly because it is a two stage low power, low noise yet high CMRR opamp with single 3 volt supply. It is a basic 3 stage amplifier with NMOS input transistors and class AB output stage. The transistor level schematic diagram is shown in Fig. 4.10.
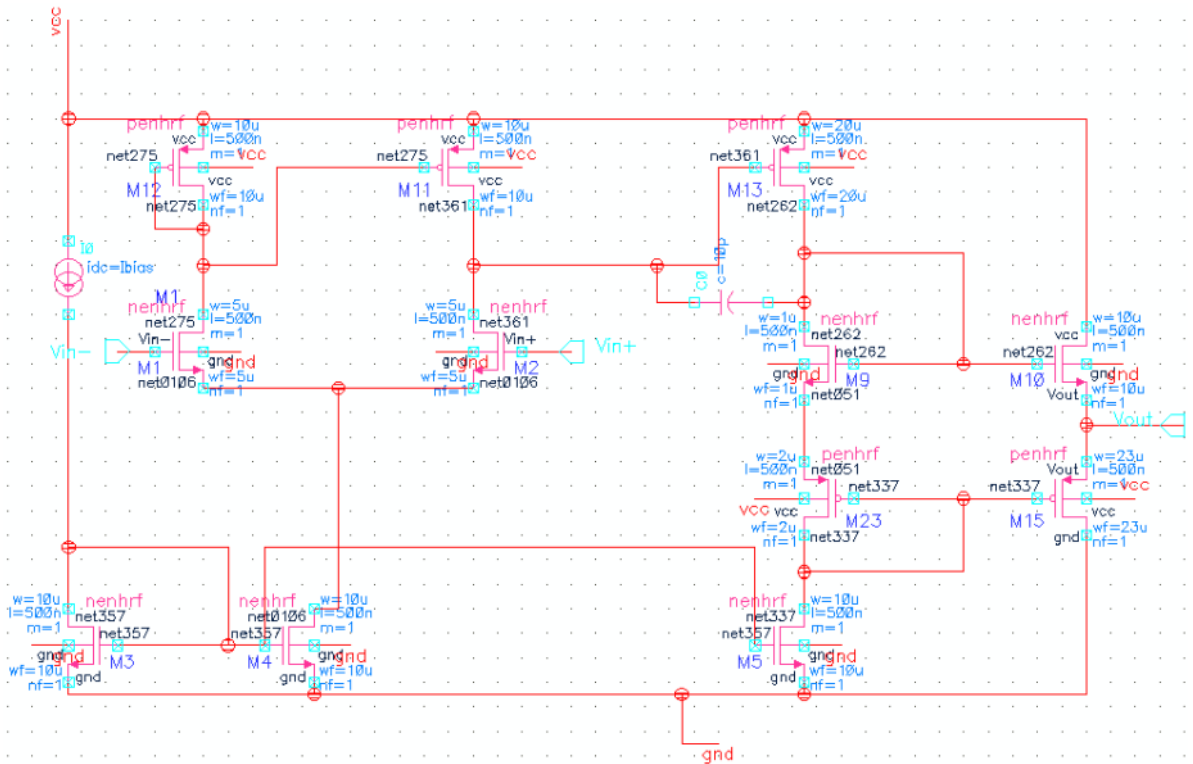

Fig. 4.10. Transistor Level Schematic Diagram

First the design equations are established to calculate parameters of OPAMP. Two stage amplification gives total differential gain equals:

$$A_{dm} = A_1 A_{13} = (\frac{R_{o1}}{rm_1})(\frac{R_{o13}}{rm_{13}})$$

rm is reciprocal of transconductance gm and Ro is output resistance of each stage, in both stage they are calculated by:

$$rm = \frac{1}{\sqrt{\mu c_{ox} \frac{W}{L} I_{bias}}}$$

$$R_o = r_{op} // r_{on} = \frac{\frac{1}{\lambda_n} + v_{DS}}{I_{bias}} // \frac{\frac{1}{\lambda_p} + v_{DS}}{I_{bias}} \approx \frac{1}{\lambda_n I_{bias}} // \frac{1}{\lambda_p I_{bias}}$$

The output stage is in class AB, provides OPAMP with enough output voltage range and small output impedance.

In order to maintain stability, compensation capacitor is added between first and second stages. The compensation (feedback) capacitor is also used to control the Gain-Bandwidth (GBW) product of the core amplifier and in turn the bandwidth of the amplifier. It is important that the bandwidth of the amplifier be made at least twice the highest working frequency for signal quality. With the W/L parameters set as below we get the desired OPAMP simulation result.

MOSFET	W/L
M1,M2	10
M3,M4,M5,M11,M12	20
M13	40
M9	2
M23	4
M10	20
M15	46

Table. 4.3. W/L ratio of OPAMP MOSFETs
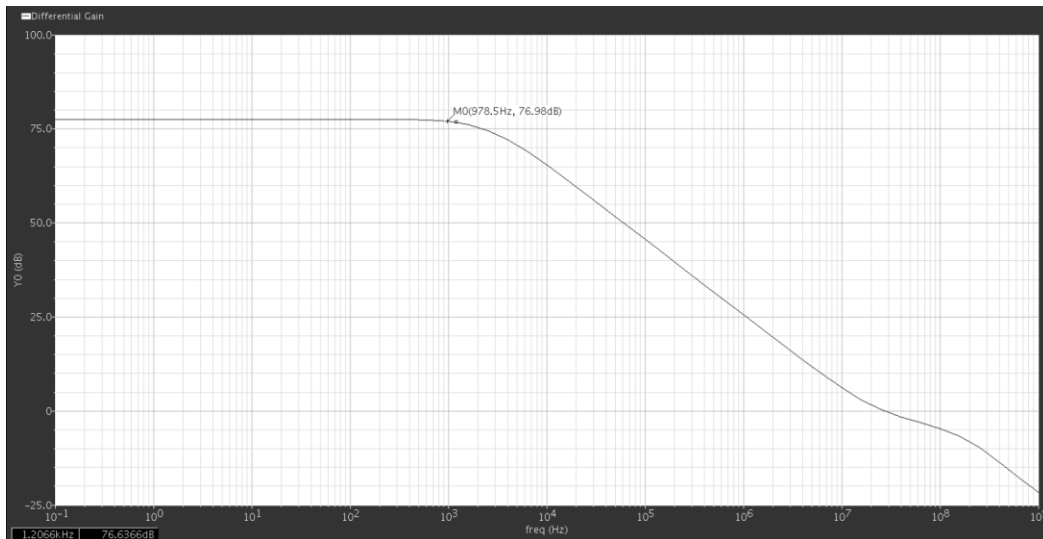
(a) Gain and bandwidth.
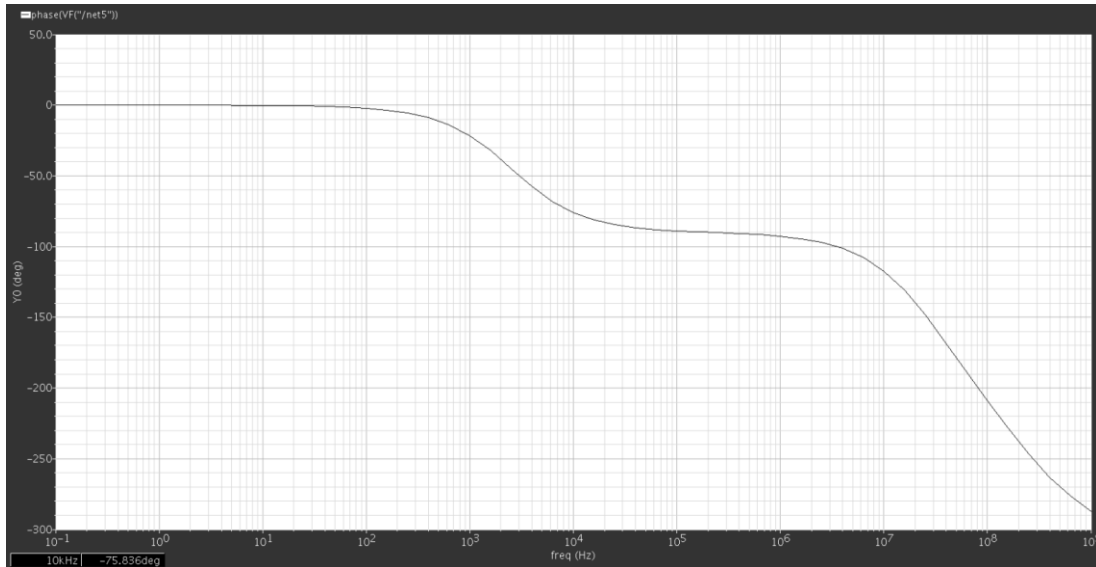
(b) Phase shift.

Fig. 4.11. Differential Frequency Response of Designed OPAMP (a) Gain and bandwidth. (b) Phase shift.

4.3.2 INA design

Based on above OPAMP cell, an instrumentation amplifier is built as shown in Fig. 4.12. OPAMP 1 and OPAMP 2 act as input buffer with differential gain set by R1 and R2 but unity common mode gain. OPAMP 3 works as normal differential amplifier so as to transform the differential output to single output, and it also has certain low-pass filtering function.
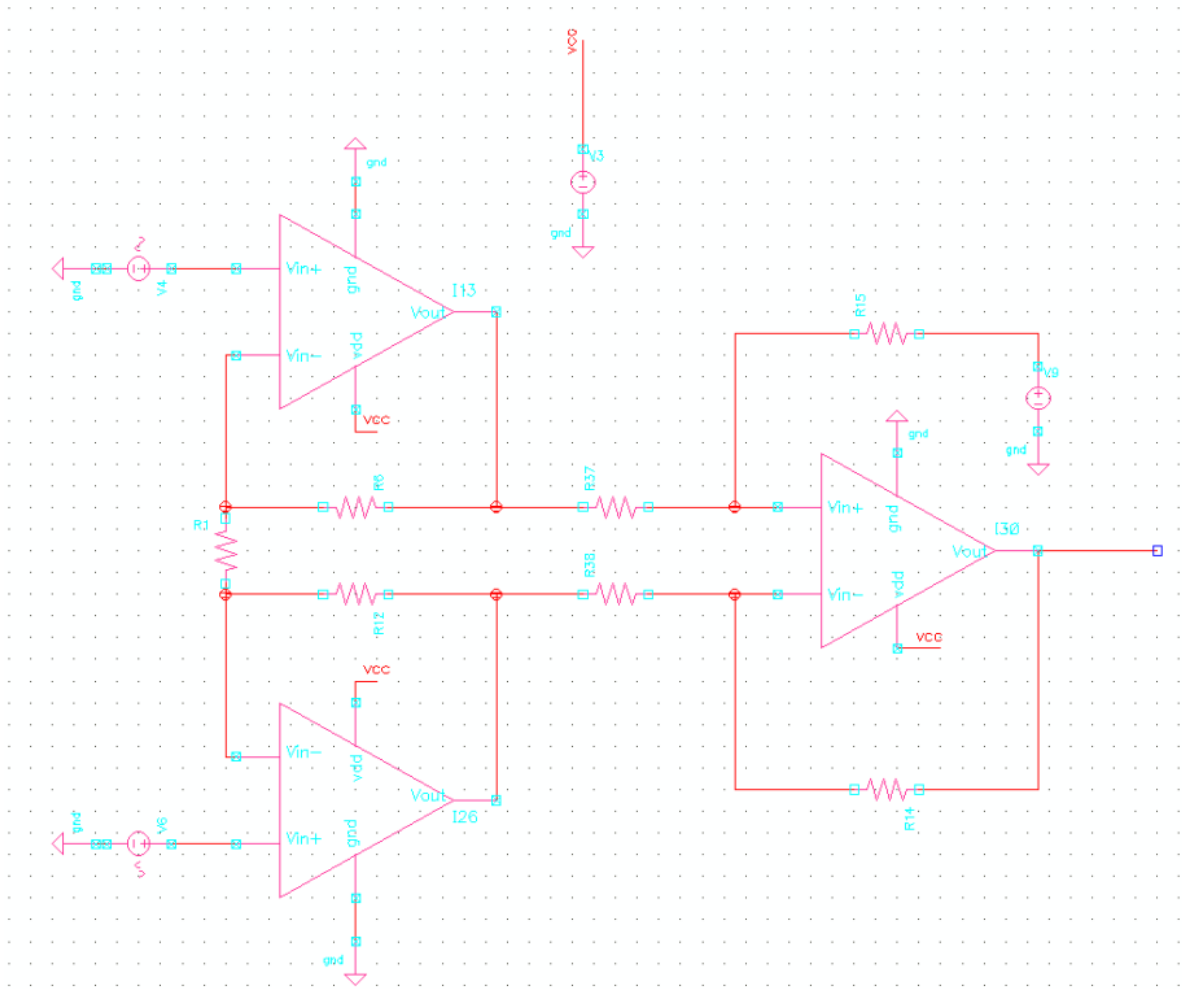
Fig. 4.12. Schematic of a Three-Op-Amp INA in Cadence

As discussed above, first stage gain is set by resistor R1 and R2, and second stage gain is set by R3 and R4:

$$A_{dm} = (1 + \frac{2R_2}{R_1})(\frac{R_4}{R_3}) = 1000(\tfrac{V}{V})$$

Gain requirement is easily satisfied with both amplification stage. Effective bandwidth can also be adjusted in single OPAMP cell by compensation capacitor.
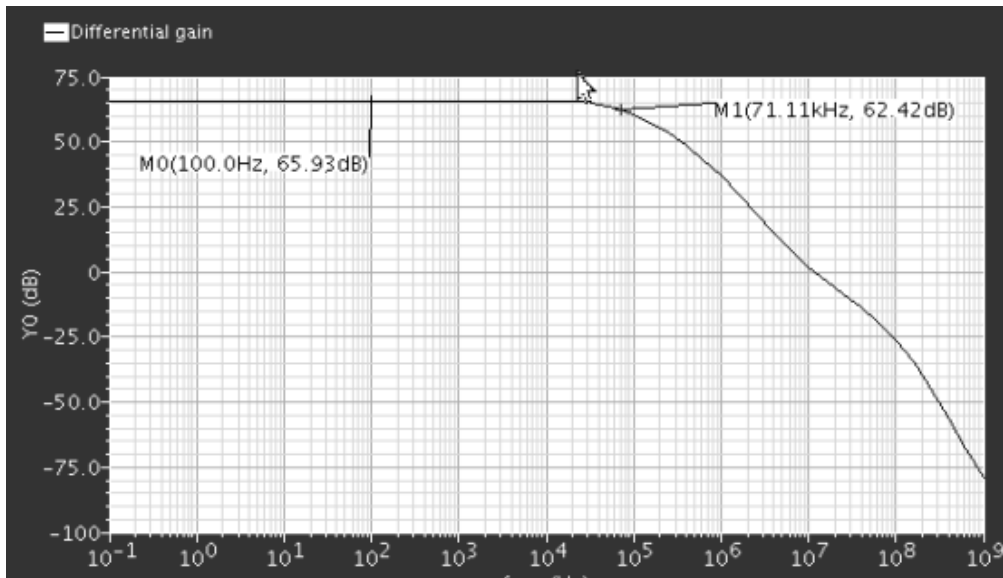
(a) Differential mode gain
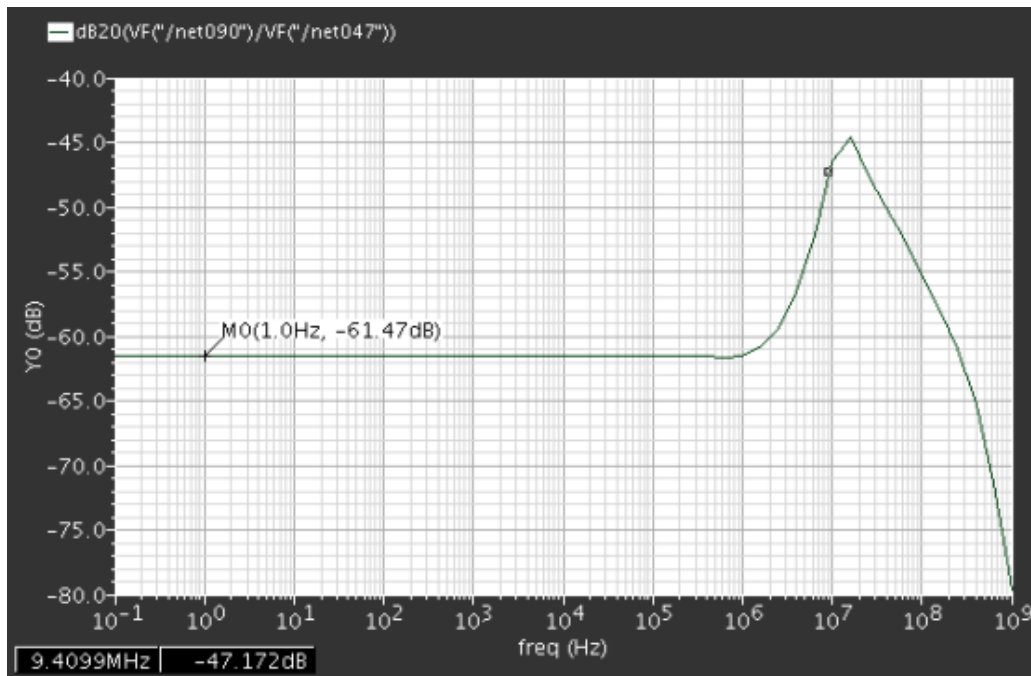
(b) Common mode gain
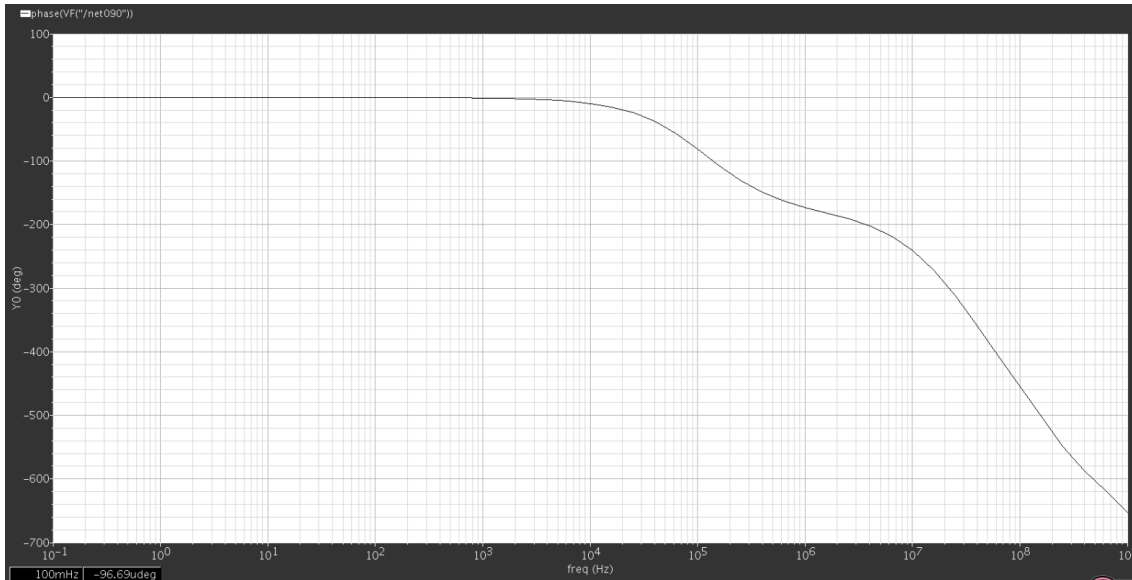
(c) Phase shift

Fig. 4.13. AC simulation result of Three-Op-Amp INA in cadence, (a) differential gain (b) common mode gain and (c) phase.

Simulation result in Fig. 4.13 is consistent with calculation. A total of 65.8dB gain with fT up to 60k Hz is achieved, enough for signal amplification and further modification.

Measured input impedance is 500M Ω at 100Hz and CMRR in desired frequency band is calculated as:

$$CMRR = \frac{A_{dm}}{A_{com}} = 65.8 - (-61.5) = 127.3dB$$

So, an instrumentation amplifier with 3 OPAMP structure is achieved with desired gain and bandwidth. Further enhancement on CMRR could be achieved with higher first stage gain.

4.3.3 Noise consideration and chopper stabilization

Due to the low amplitude and low frequency nature, EEG signal is extremely prone to be contaminated by system noise. Since OPAMP cells are used as input buffers in the first stage, their noise factors dominants whole system signal to noise ratio. Thus, for desired EEG SNR, noise contributions of an OPAMP is analyzed, methods for minimizing them are compared.

4.3.3.1 Noise in OPAMP

The total equivalent input-referred noise power is used for evaluating noise performance of circuit. For the single OPAMP illustrated in Figure 4.10, the dominant noise contributors for are the input NMOS transistors, M1 (M2) and the PMOS load transistors, M11 (M12).

For single common source stage, output noise current density and voltage power are calculated as:

$$I_{N,out}^2 = I_{N,th}^2 + I_{N,1/f}^2 = 4 \cdot k \cdot T(\frac{2}{3}g_m) + \frac{K \cdot g_m^2}{C_{ox} \cdot W \cdot L \cdot f}$$

$$V_{N,out}^2 = I_{N,tot}^2 \cdot (r_{o1} // r_{o12})$$

Considering half of differential loop and neglecting noise contribution of transistor M4:

$$V_{N,tot}^2 = V_{N(M1)}^2 + V_{N(M12)}^2 + \frac{V_{N(M9)}^2 + V_{N(M13)}^2}{g_{m13} \cdot (r_{o13} // r_{o9})}$$

Contribution of second stage noise can be neglect because it is divided by the gain of both first stage and second stage. The resulting input-referred noise power can then be derived to:

$$V_{N,in}^2 = 4 \cdot k \cdot T \frac{2}{3}(\frac{1}{g_{m1}} + \frac{g_{m12}}{g_{m1}^2}) + \frac{1}{C_{ox}}[\frac{K_p \cdot g_{m12}^2}{(WL)_{12} \cdot g_{m1}^2} + \frac{K_p}{(WL)_1}]\frac{1}{f}$$

In them, thermal noise contribution is:

$$V_{Nin,th}^2 = 4 \cdot k \cdot T(\frac{2}{3g_{m1}} + \frac{2g_{m12}}{3g_{m1}^2})$$

Flicker noise contribution equals:

$$V_{Nin,1/f}^2 = \frac{1}{C_{ox}}[\frac{K_p \cdot g_{m12}^2}{(WL)_{12} \cdot g_{m1}^2} + \frac{K_N}{(WL)_1}]\frac{1}{f}$$

From above equations, we can see clearly that at low frequency range, the noise spectrum is dominated by flicker (1/ f) noise. As the frequency goes higher, the noise spectrum is determined by the thermal noise of the transistors. Unfortunately, the entire desired EEG signal frequency band (0.1 Hz to 100 Hz) lies in low frequency region thus would be heavily contaminated by flicker noise without doubt. Noise simulation is done for single OPAMP as shown in Fig. 4.14. The 1/f noise ranges from 22.92uV/sqrt(Hz) to 695nV/sqrt(Hz) within 0.1 Hz to 100 Hz. Which made the acquiring of low amplitude EEG signal nearly impossible.
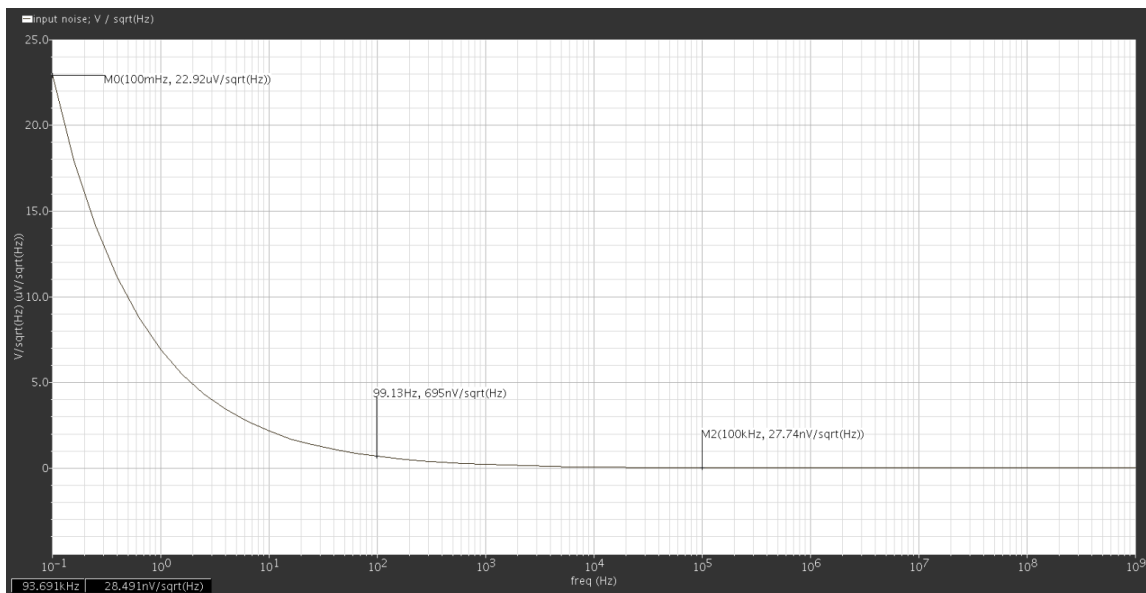

Fig. 4.14. Cadence simulation result of single OPAMP input referred noise spectral

Certain methods could be applied in order to minimize the 1/f noise, such as choice of using PFETs in the OPAMP input stage since KVP << KVN. Also, making L12 (load device length) greater than L1 (input device length) will reduce the overall flicker noise contribution of the OPAMP. In addition, making the devices larger would also minimize the noise. However for low noise levels necessitated by the weak input signal, the large device dimensions would lead to poor PSRR at higher frequencies due to parasitic feedthrough [29]. For an acceptable SNR of such low frequency band, all these approaches could only be succeed at huge expanse. To overcome this limitation a chopper stabilization technique is utilized in this work for low frequency EEG signal acquiring.

4.3.3.2 Chopper Stabilization technique

A chopper stabilized INA shown in Fig. 4.15 uses modulation to transpose the desired signal band to a higher frequency band. Higher frequency signal would be amplified with much less 1/f noise. A demodulator then translates the desired signal band back to base band.
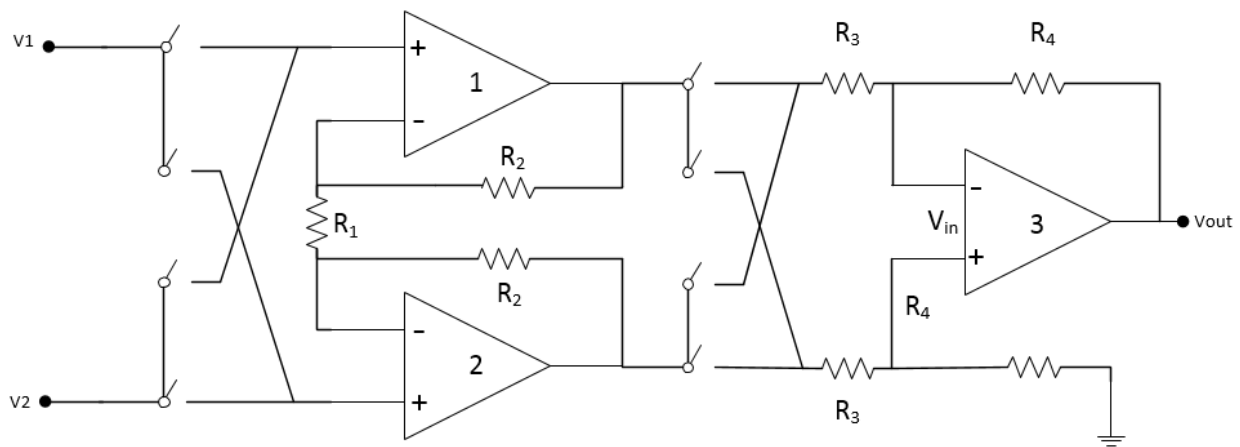

Figure 4.15. Schematic of chopper stabilized INA

The input signal is first modulated with chopping frequency. The chopper carrier is a square wave which can represent by Fourier series below:

$$X_{aquare}(t) = \frac{4}{\pi} \sum_{k=1}^{\infty} \frac{\sin((2k-1) \cdot 2\pi f_c t)}{2k-1} = \frac{4}{\pi}(\sin(2\pi f_c t) + \frac{1}{3}\sin(6\pi f_c t) + \frac{1}{5}\sin(10\pi f_c t) + \cdots)$$

Here f_c is the chopping frequency. It is usually choose higher than the corner frequency which is the frequency at which the 1/ f noise is equal to the thermal noise. The noise corner of MOSFET usually located at several kHz. From Figure 3.2.3.1.5 it's about 10 kHz so in this work chopping frequency is chosen to be 50 kHz whose harmonics are easier to be filtered with anti-aliasing filter.

This technique can be seen as input signal being convolved with the odd harmonics frequencies of the modulation signal. After amplification, same chopping frequency then shifting signal back to the baseband. However, during the process the amplifier noise is only chopped once, which will shift the 1/ f -noise to the odd multiples of the chopping frequency as illustrated in in Fig. 4.16, leaving the thermal noise as the main in-band noise contributor.
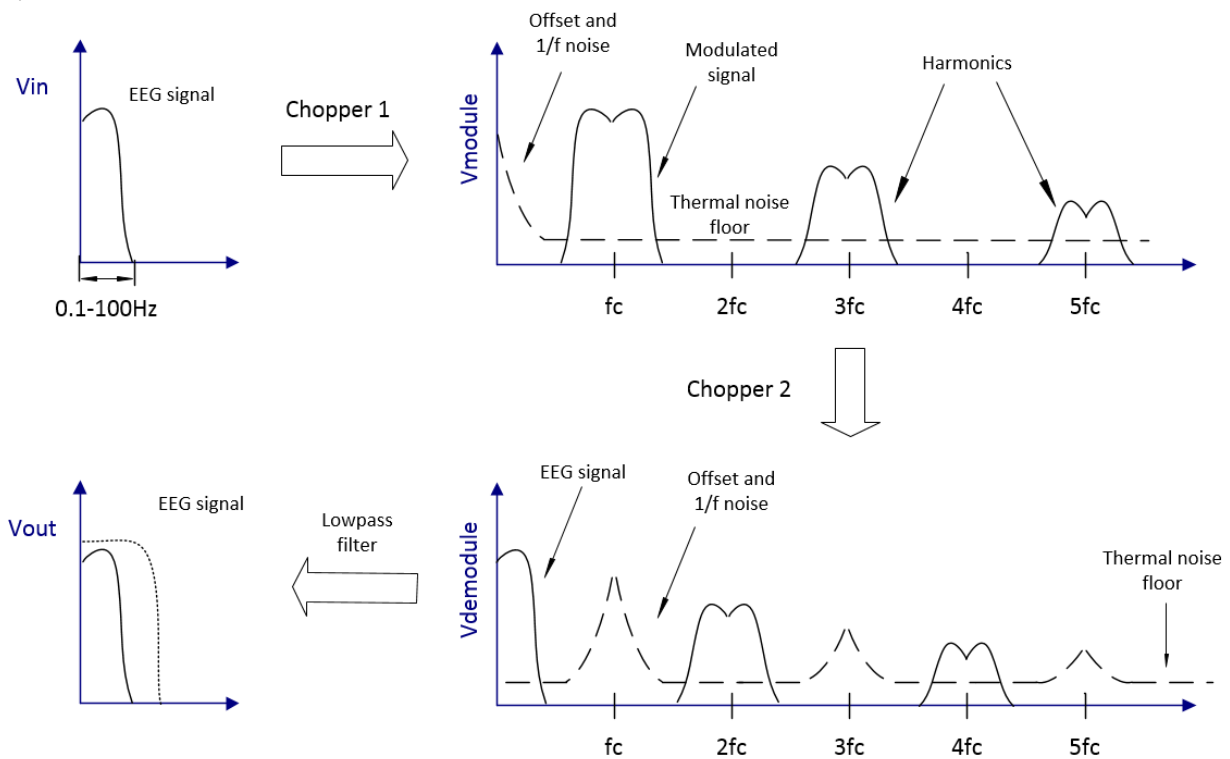
Fig. 4.16. Principle of Chopper Stabilization

4.3.3.3 Passive chopper design

Passive chopper circuits are easily implemented in MOS technology as only four switches are needed for a fully differential chopper [30]. As shown in Fig. 4.17. CMOS switches are used for linear on-resistance of input signal region and also to reduce the charge injection effect.

For fast switch clock waveforms, the channel charge infection cannot be eliminated by single complementary PMOS and NMOS pairs. Hence one more half sized dummy CMOS switch with shorted drain-source are inserted in the signal path to further compensate for the charge injection. They are working in the counterphase clock, "open" at the same time when the real switches are closed, absorbing injected charges.

As the input signal now interface chopper circuit directly but not INA buffers, the switch becomes noise critical. W/L is set to be 10/1 for PMOS and 4/1 for NMOS for low on resistance.
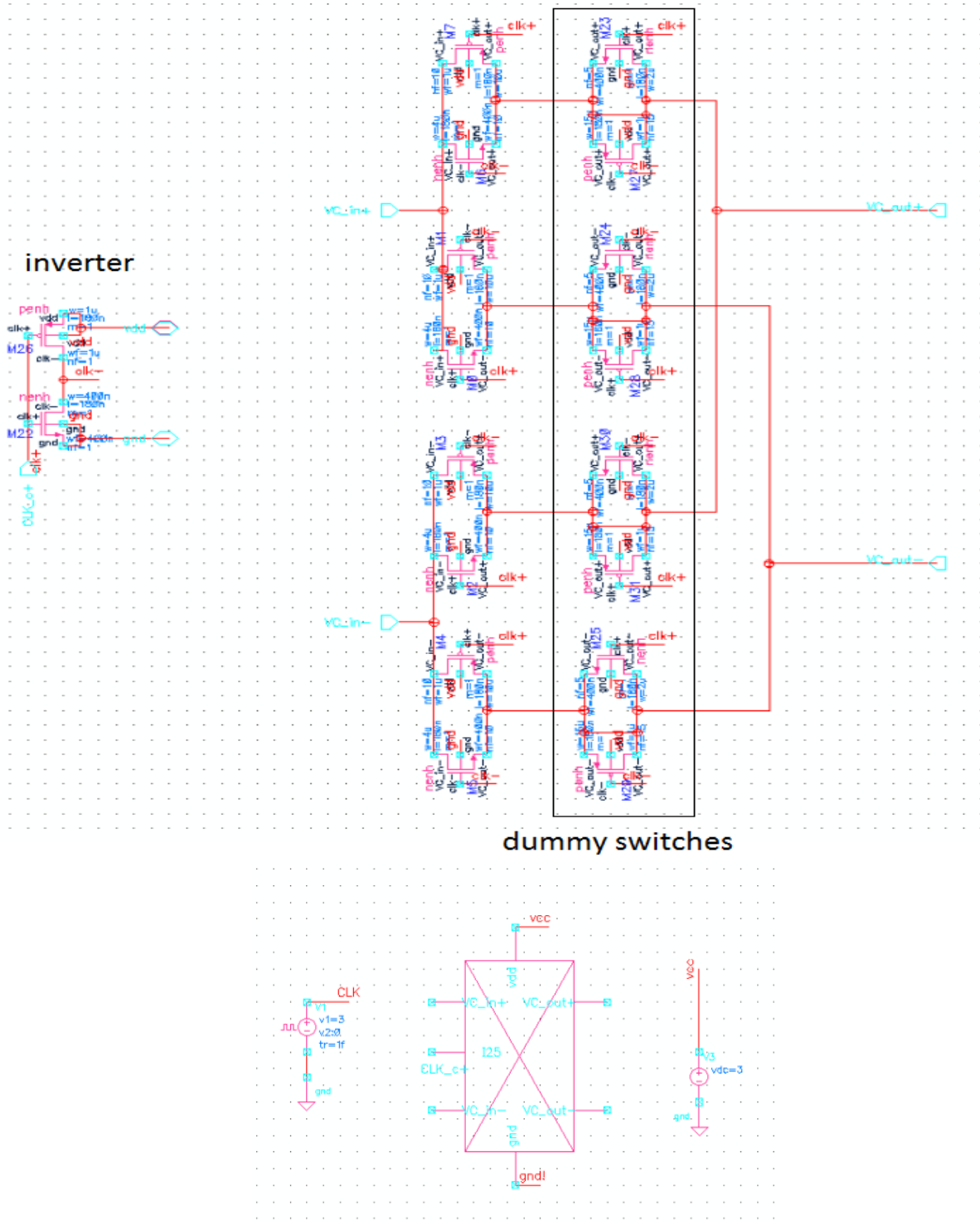

Fig. 4.17. Chopper realized by Inverter and CMOS switches

53

4.4 Signal bandwidth consideration

4.4.1 First order high pass filter

Due to the large DC-offsets may be present at the cuff electrode outputs, the first stage is AC-coupled. With coupling capacitor and a grounding resister added, the input OPAMP buffer also functioning as a first order high pass filter as shown in Figure 4.18.
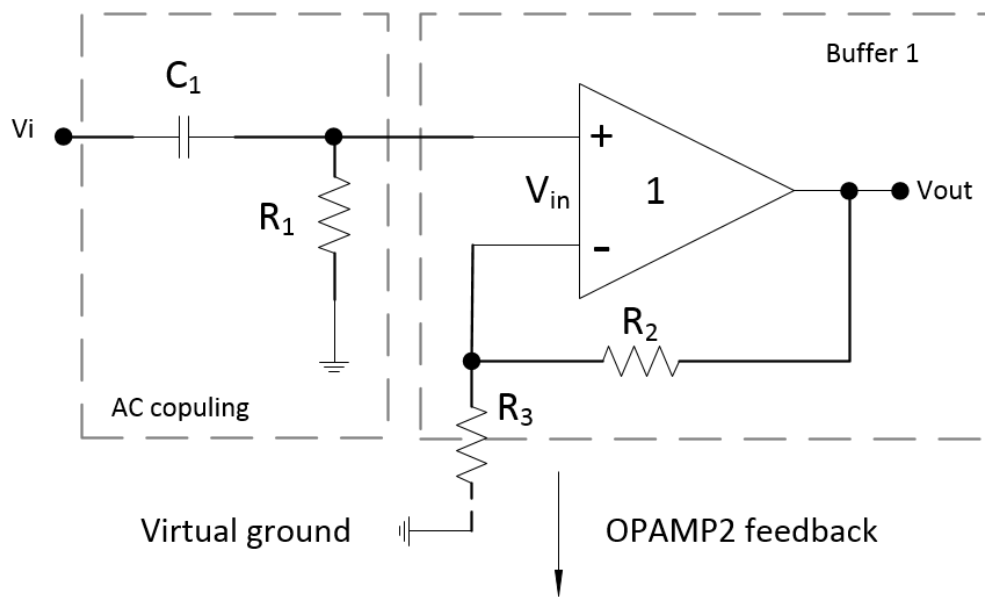

Fig. 4.18. First order High-Pass filter

High pass cutoff frequency can be calculate as:

$$f_{cutoff} = \frac{1}{2\pi R_1 C_1}$$

For cutoff frequency of 0.1 Hz as input signal required. When C1 set to 5 nP, R1 should be:

$$R_1 = \frac{1}{2\pi C_1 f_{cutoff}} = 318M\Omega$$

Simulation results are shown in Figure 4.19.
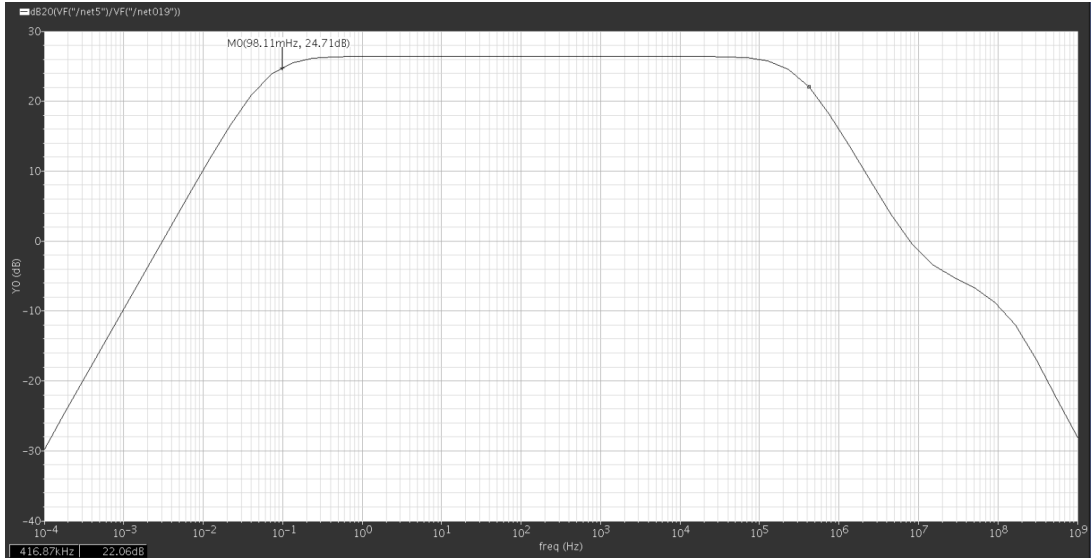
(a) Gain and bandwidth
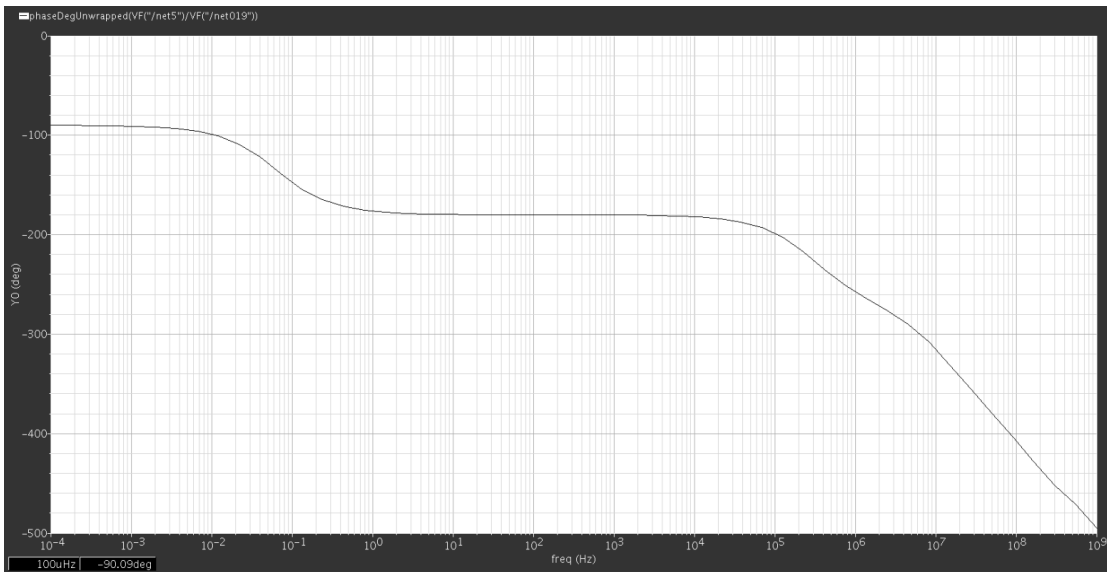
(b) Phase shift

Fig. 4.19. AC simulation results of first order High-Pass filter (a) Gain and bandwidth. (b) Phase shift.

From results we can see that the desired high pass cutoff frequency is achieved. The low pass cutoff comes from OPAMP and the filter gain is decided buffer feedback ratio.

4.4.2 Second order Sallen-Key Low-Pass filter

A second-order, continuous-time low-pass filter which provides additional gain is applied at the INA output. Low pass cutoff frequency is set to 100Hz for residue image suppression. It removes the modulated noise and artifacts as well as dynamic offset effects.
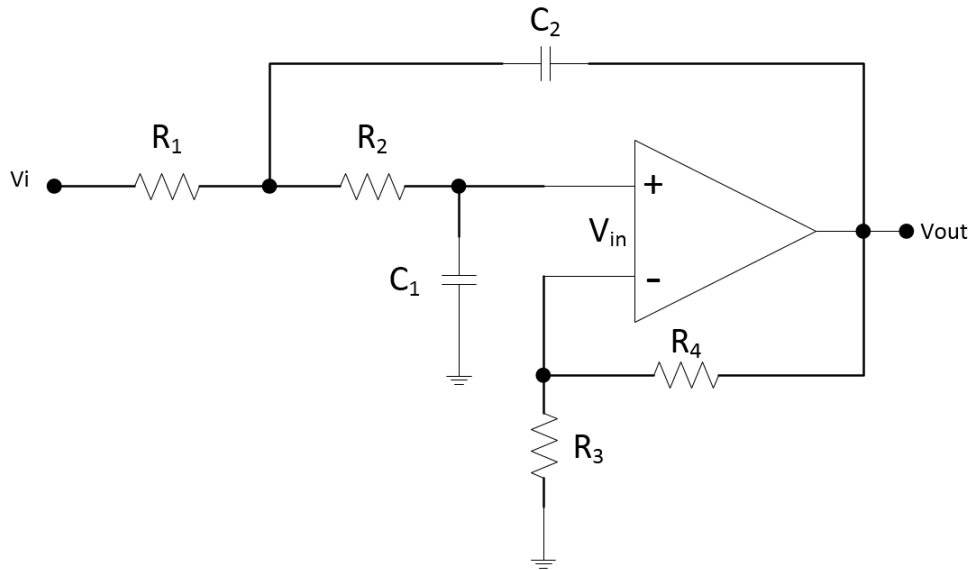

Fig. 4.20. Sallen-Key achitecture Low-Pass filter

Filter adopt Sallen-Key architecture since its simplicity to adjust and easily selectable gain. Its ideal transfer function is:

$$H(f) = \frac{\dfrac{R3+R4}{R3}}{(j2\pi f)^2(R_1R_2C_1C_2) + j2\pi f(R_1C_1 + R_2C_1 + R_1C_2(-\dfrac{R_4}{R_3})) + 1}$$

Then, with substitutions:

$$K = \frac{R3+R4}{R3}$$

$$FSF \times f_{cutoff} = \frac{1}{2\pi \sqrt{R_1 R_2 C_1 C_2}}$$

$$Q = \frac{\sqrt{R_1 R_2 C_1 C_2}}{R_1 C_1 + R_2 C_1 + R_1 C_2 (1-K)}$$

Transfer function can be expressed as standard form for second order low pass filter:

$$H_{second\_LP}(f) = \frac{K}{(\frac{f}{FSF \times f_{cutoff}})^2 + \frac{1}{Q} \frac{jf}{FSF \times f_{cutoff}} + 1}$$

f is the frequency variable, f_{cutoff} is the cutoff frequency, FSF is the frequency scaling factor, and Q is the quality factor. In this design, low pass Sallen Key filter is set to R1=R2=R and C1=C2=C for simplicity. Thus the equation simplifies to:

$$FSF \times f_{cutoff} = \frac{1}{2\pi RC} \qquad\qquad Q = \frac{1}{3-K}$$

With cutoff frequency and Q independent of each other, filter parameters can be easily set by changing R and feedback resistors. C is set to be 200pF where a 100 Hz cutoff frequency is preferred in this design. R can then be calculated as:

$$R = \frac{1}{2\pi C f_{cutoff}} = 7.961 M\Omega$$

The simulation result is shown in Fig. 4.21.
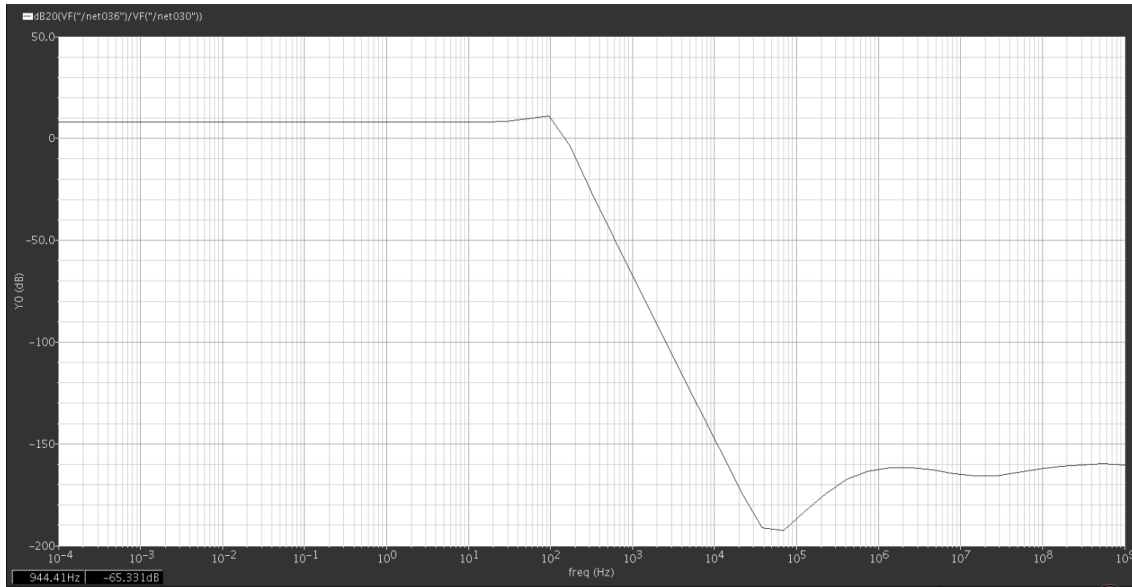
(a) Gain and bandwidth
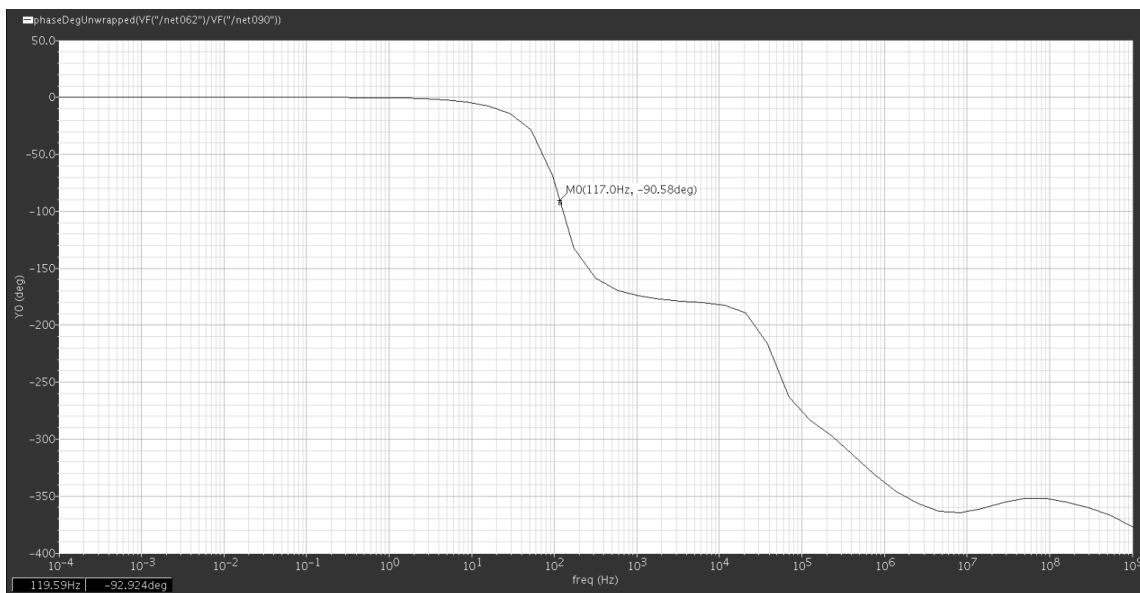
(b) Phase shift

Fig. 4.21. AC simulation results of second order Sallen-Key Low-Pass filter. (a) Gain and bandwidth. (b) Phase shift.

4.5 Complete AC coupling chopper stabilized INA with low pass filter

From the above analysis and discussion, techniques and modifications are applied on designing preamplifier for acquiring and amplifying EEG signal with better quality. We end up with an AC coupling chopper stabilized INA with second order Sallen-Key low pass filter which provides desired gain and bandwidth, high CMRR and good noise performance. Circuit schematic is illustrated in Fig. 4.22.

Simulation results are also shown in Fig. 4.23-4.27 with explanation.

Fig. 4.22.
AC coupling
chopper stabilized
INA with low pass filter

Second order Sallen-
Key Low-Pass filter

Difference amplifier
INA second stage

Demodulation
chopper

Input buffer
INA first stage

Modulation
chopper

Input signal and
AC coupling

60
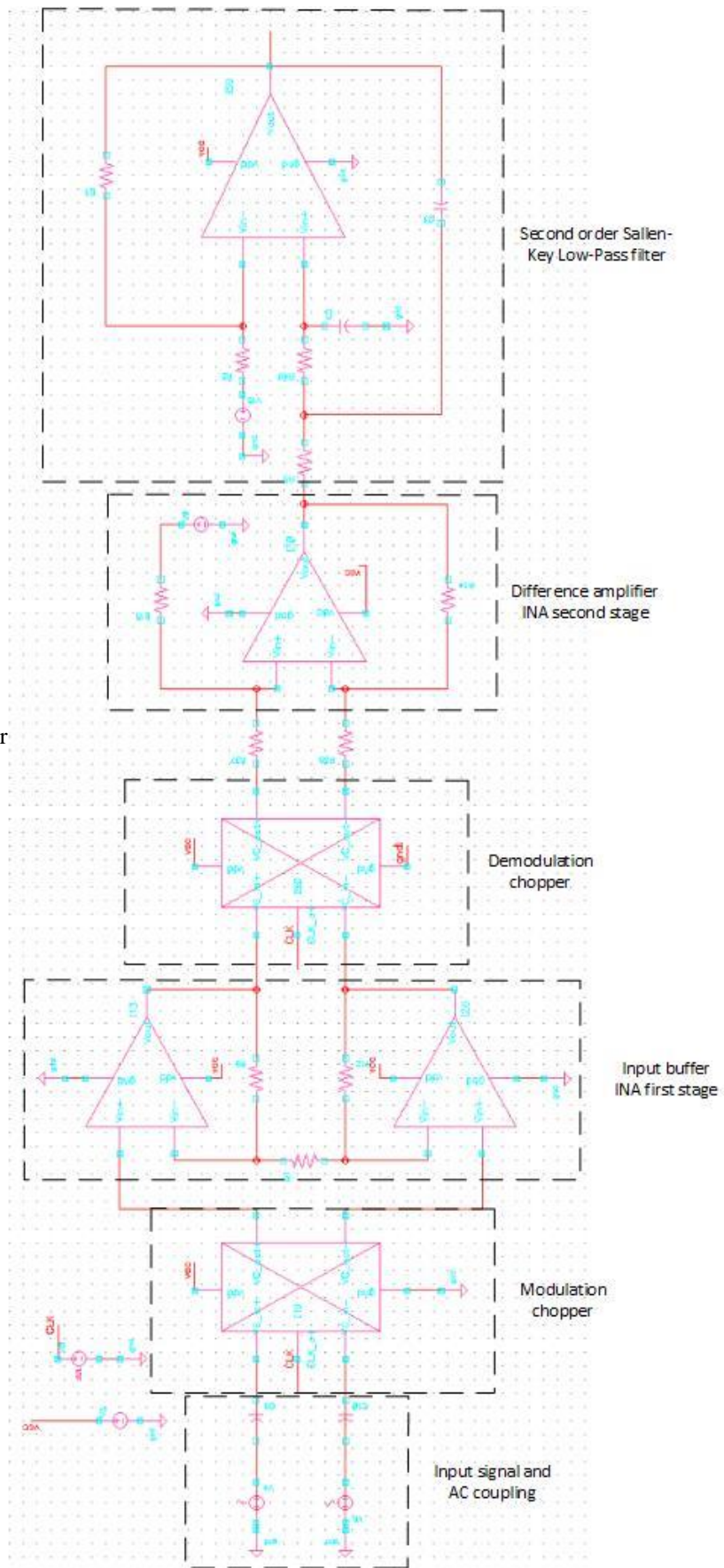
To simulate EEG signal from measuring electrodes, two pairs of input signals are compared. First pair of input signals are set to be differential sin wave with 180 degree phase difference, both in 100Hz and have 20uV peak-peak voltage. Second pair of input signals are set to be 100Hz in phase sin wave with 20uV peak-peak voltage difference (Vpp=10uV in input 1 and Vpp=30uV in input 2). Their input differential signal and simulation results are same.

Common mode signal are simulated as DC offset in both pair of input signals with different value range from 10uV to 100mV.

Before first chopper, DC offset is filtered out perfectly by high pass filter even they with different value (50mVdc in input 1 and 100mVdc in input 2). Differential EEG signal is then modulated to chopper frequency before amplification as shown in Fig. 4.23.
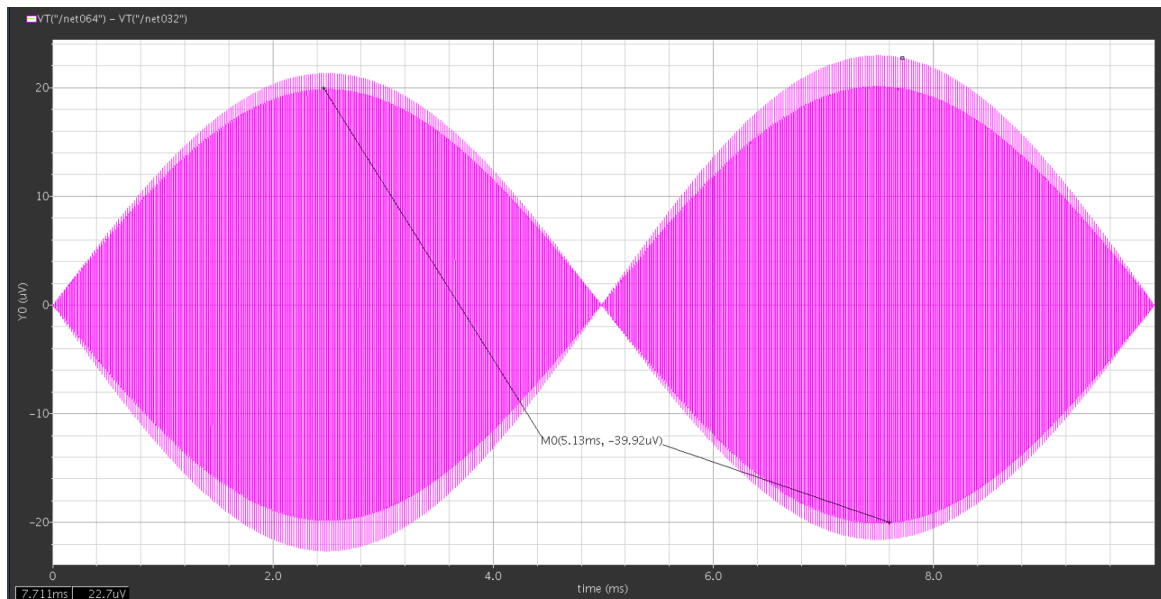

Fig. 4.23. Modulated signal

61

Modulated differential signal is then amplified by INA first stage with much lower 1/f noise thus has better SNR and is ideal for further process.
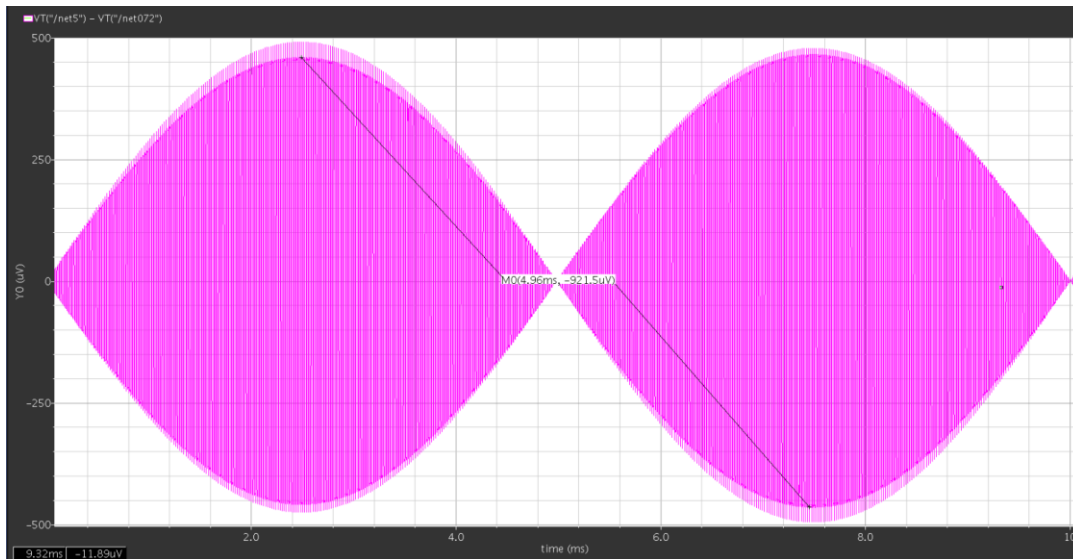

Fig. 4.24. First stage amplification

Signal is then demodulated by second chopper and further amplified in INA second stage differential amplifier. The amplifier also has low pass cutoff effect and filtered partial of signal and noise image as shown in Fig. 4.26. However, for clean amplified EEG signal, higher order low pass filter with right cutoff frequency is still needed.
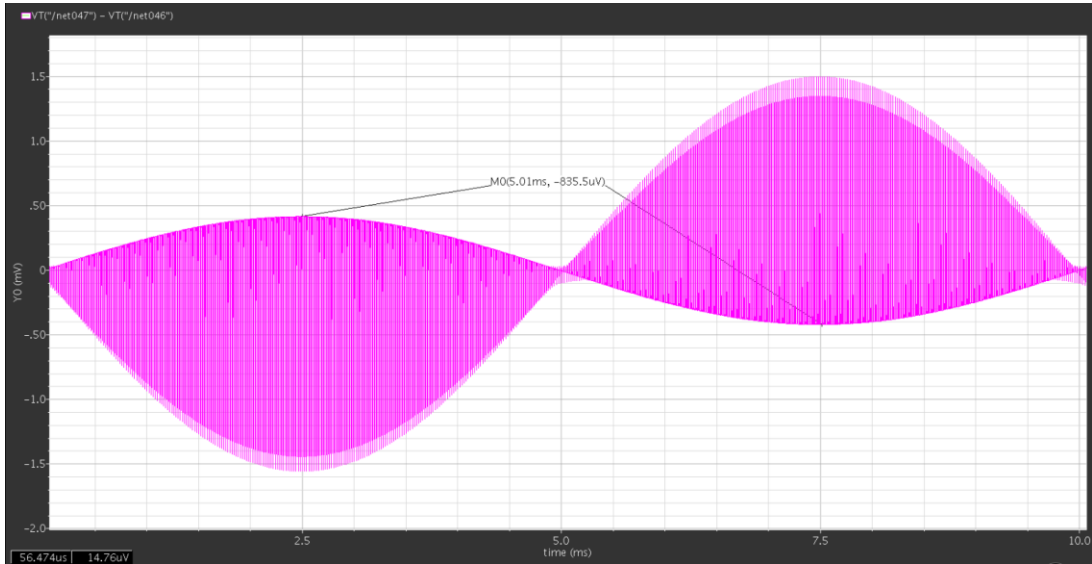
Fig. 4.25. Demodulated signal
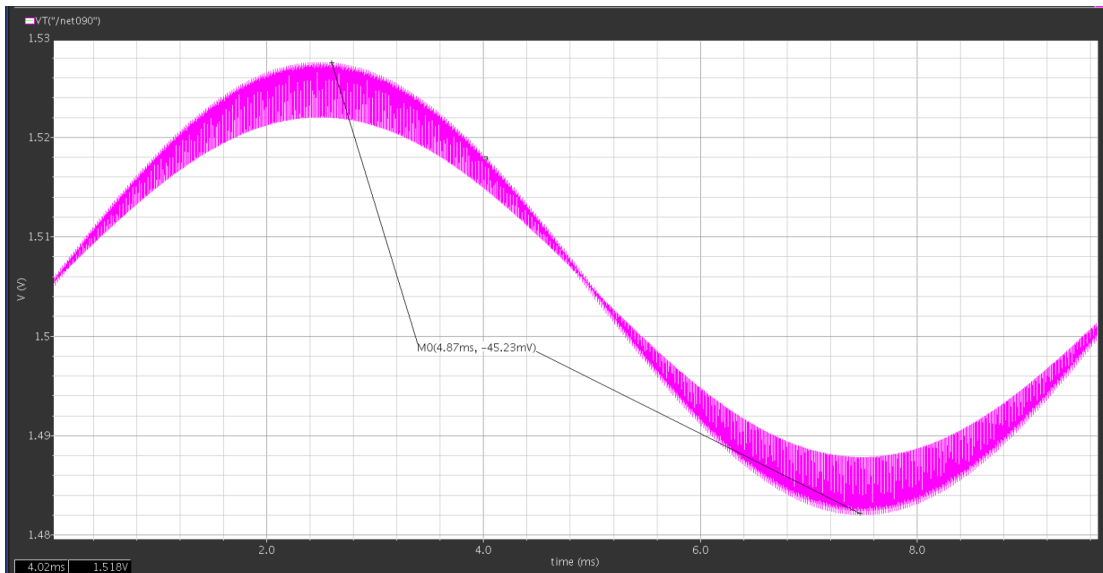
Fig. 4.26. INA output signal

With two second order low pass filter, the undesired images of chopper and noise in INA output signal are filtered out leaves clean EEG signal as shown in Fig. 4.27 and Fig. 4.28.
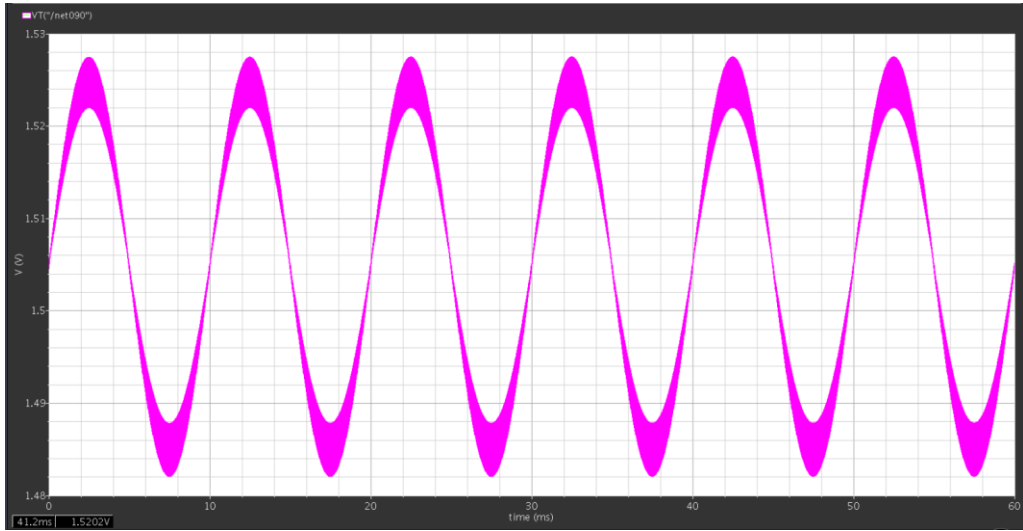
Fig. 4.27. INA output signal with undesired high frequency components
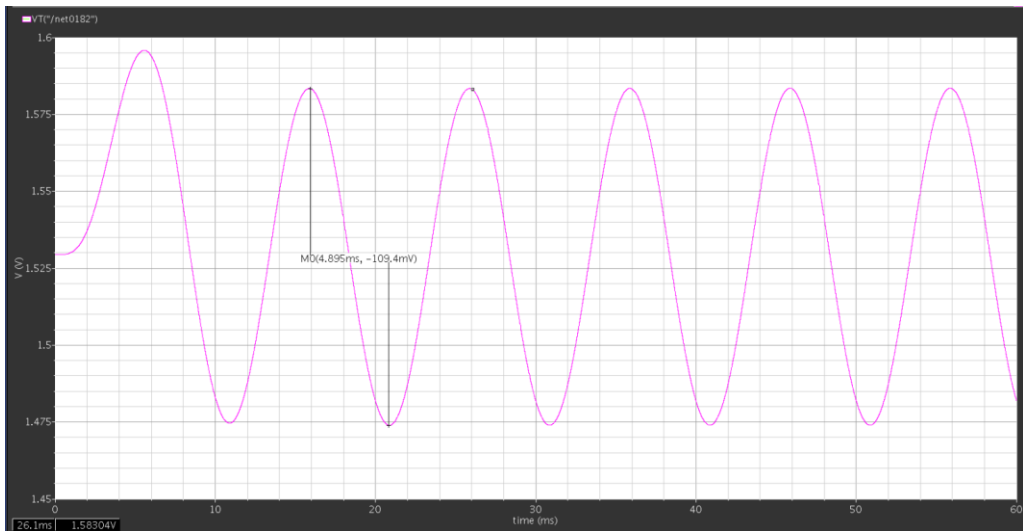
Fig. 4.28. Clean output EEG signal after filter
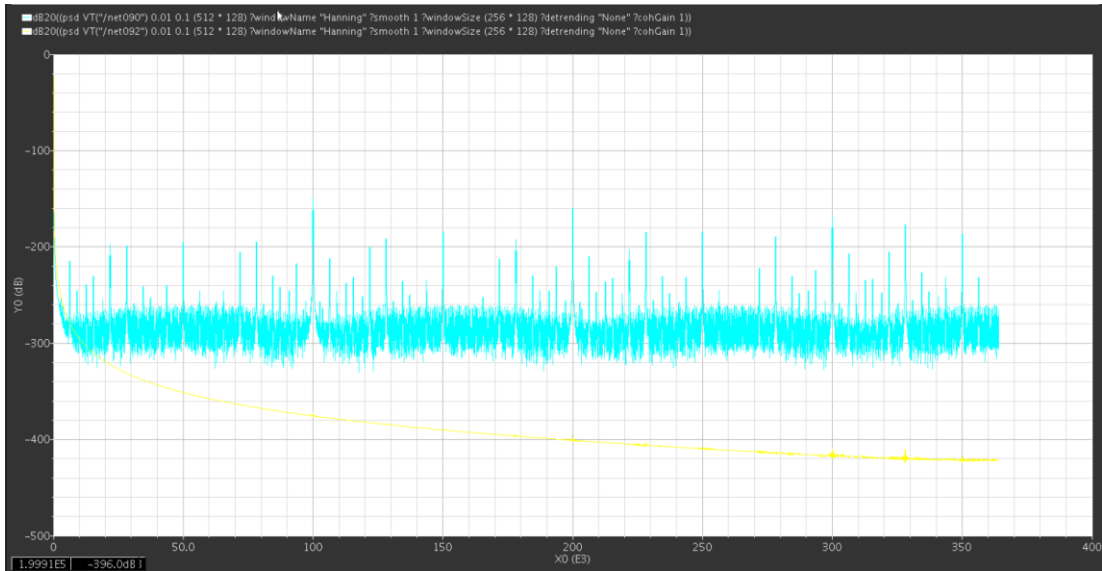
Fig. 4.29. Frequency domain of INA output signal (in blue) and signal after filter (in yellow)
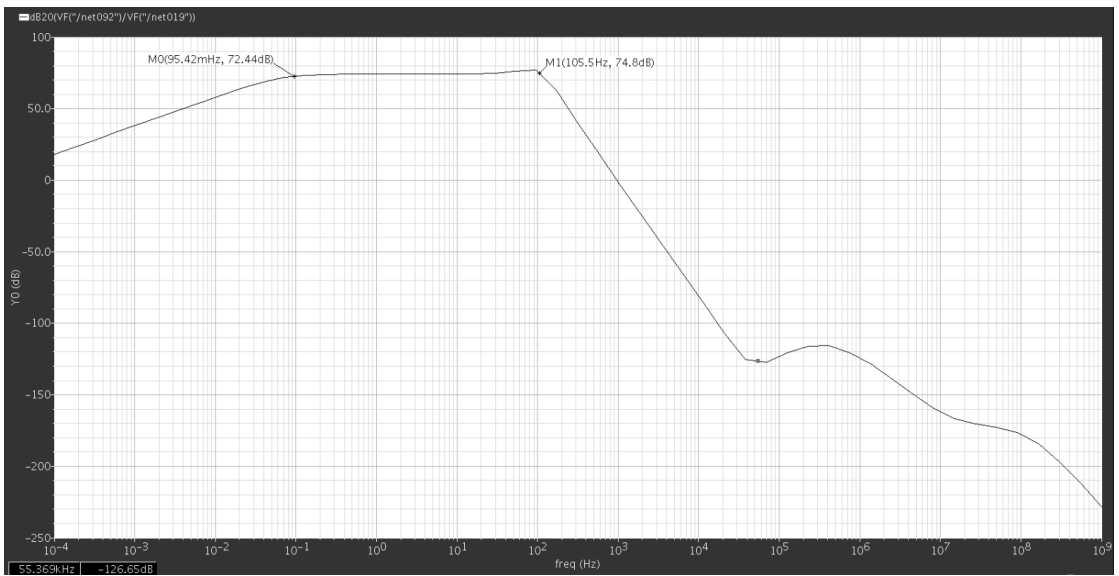
Fig. 4.30. System gain and bandwidth
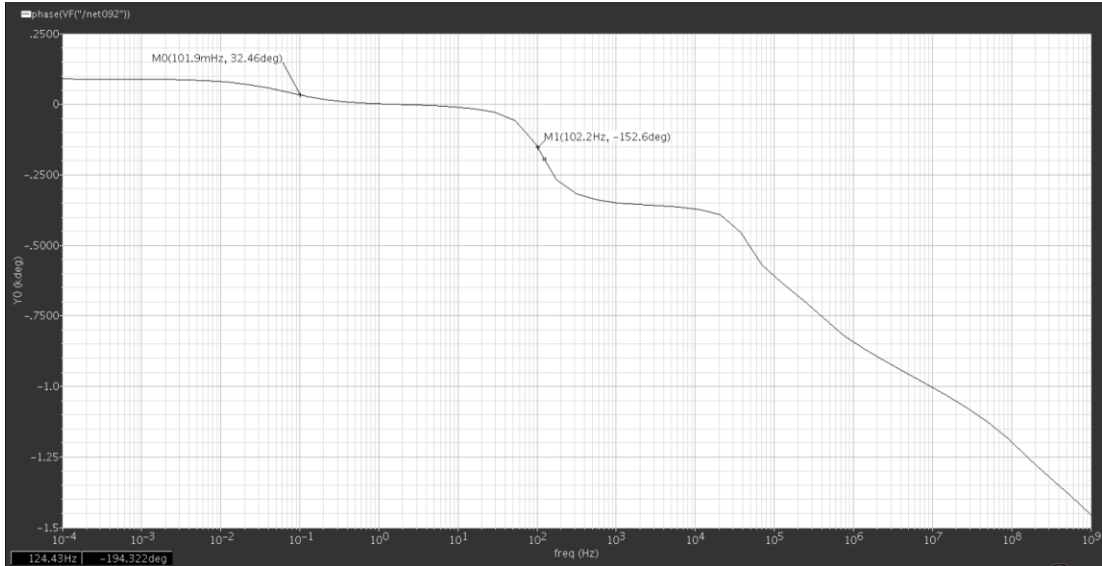
Fig. 4.31. System phase shift
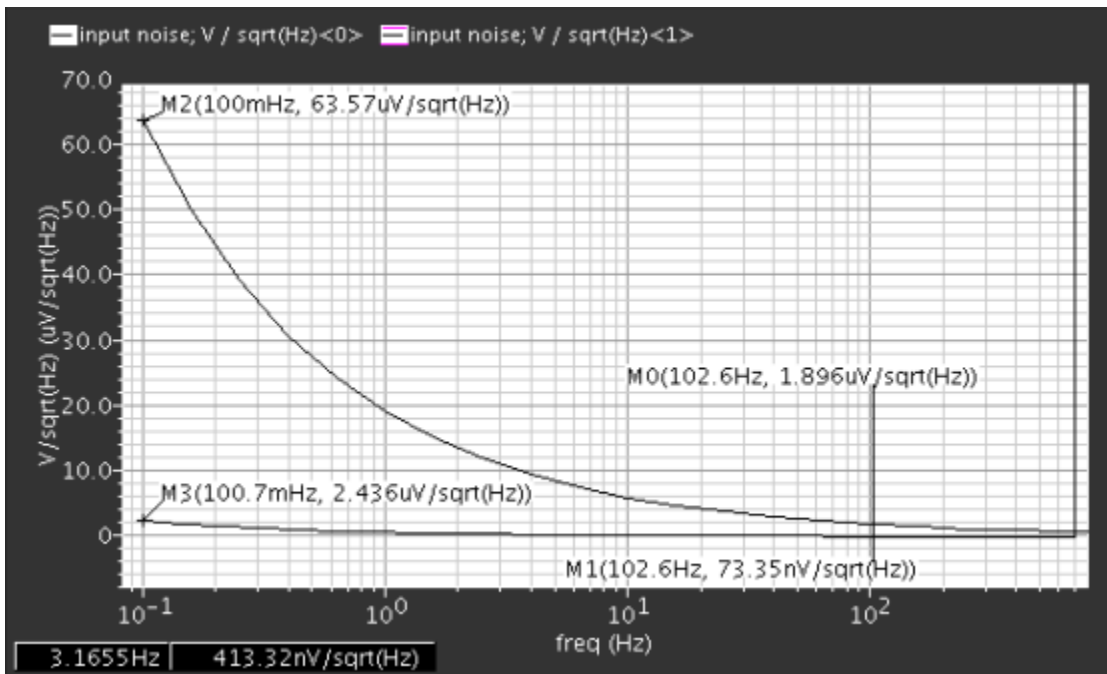
Fig. 4.32. System Input noise with and without chopper stabilization

66

4.6 Summary

For improving acquired EEG signal quality in simultaneous MRI/EEG recording, a MRI electromagnetic environment compatible EEG signal acquiring SOC is proposed. Preamplifier which is the key component in deciding EEG SNR in frond end was discussed in detail. As result, an AC coupling chopper stabilized INA with low pass filter was implemented in 0.18um SiGe (BCS180G) technology and simulated in cadence. Results shown that the preamplifier provides enough differential gain and CMRR over desired bandwidth, input referred noise was dramatically decreased by chopper stabilization technique.

Chapter 5 Conclusion and future work

5.1 Conclusion

In this thesis, MRI electromagnetic environment is introduced and its influences on EEG recording system is analyzed in detail. Discussion on MRI electromagnetic influences on semiconductor devices revealed the possibility of in-bore EEG signal requiring system. Then, an amplifier suitable for amplifying EEG signals with improved SNR has been presented. Noise performance improvement is achieved through the use of chopper modulation for low-frequency 1/ f noise removal. Ideal differential gain and CMRR is achieved with three OPAMP INA, thus ensure correct operation when facing large common mode interferers. With the input AC coupling high pass filter and second order output low pass filter, clean output signal was get with desired signal bandwidth.

5.2 future work

Future work would be first focusing on improvement on preamplifier. (1) OPAMP of INA first stage change could use BJTs instead of MOSFETs for better noise performance. (2) Lower power consumption could be achieved by using lower supply voltage and adjusting biasing currents for different parts, for example more area and higher biasing current in first stage for better noise performance and gain but lower biasing current in second stage amplifier and filter OPAMPs. (3) Resisters used in system can be achieved by using diode MOSFETS for more accuracy and less chip area. (4) Also, bandgap reference should be applied for better Power Supply Rejection Ratio and circuit stability.

Secondly, development and implementation of the whole system function is the long time goal, more parts will be designed for further signal processing.

Bibliography

1. V. Menon and S. Crottaz-Herbette. "COMBINED EEG AND FMRI STUDIES OF HUMAN BRAIN FUNCTION". INTERNATIONAL REVIEW OF NEUROBIOLOGY, VOL. 66 DOI: 10.1016/S0074-7742(05)66010-2, 2005

2. Lemieux, L., Allen, P.J., Franconi, F., Symms, M.R., Fish, D.R., 1997. "Recording of EEG during fMRI experiments: patient safety". Magnetic Resonance in Medicine 38, 943 – 952.

3 P .J. Allen, G. Polizzi, K. Krakow, D.R. Fish, L. Lemieux, Identification of EEG events in the MR scanner: the problem of pulse artifact and a method for its subtraction, Neuroimage 8 (1998) 229–239.

4. A. Perrin and M. Souques. "MRI and Static Electric and Magnetic Fields". Electromagnetic Fields, Environment and Health,DOI: 10.1007/978-2-8178-0363-0_2, _ Springer-Verlag France 2012

5. D. Mantini, M.G. Perrucci, S.Cugini, A.Ferretti, G.l. Romani, and C. Del Gratta. "Complete artifact removal for EEG recorded during continuous fMRI using independent component analysis" NeurOiMAGE 34 (2007) 598-607

6. McRobbie, D.W.; Moore, E.A.; Graves, M.J.; Prince, M.R. MRI – "From Picture to Proton". Cambridge University Press: Cambridge, New York, USA, 2006.

7. International Electrotechnical Commission. IEC Standard 60601-2-33. Particular requirements for the safety of magnetic resonance equipment for medical diagnosis. International Electrotechnical Commission, 2002.

8. Lajos Losonczi , László F. Márton. "Embedded EEG signal acquisition systems". The 7th International Conference Interdisciplinarity in Engineering, INTER-ENG 2013, 10-11 October 2013, Petru Maior University of Tirgu Mures, Romania

9. Petra Ritter, Arno Villringer. "Simultaneous EEG – fMRI". Neuroscience and Biobehavioral Reviews 30 (2006) 823 – 838

10. A. Salek-Haddadi, K.J. Friston, L. Lemieux, D.R. Fish, "Studying spontaneous EEG activity with fMRI". Brain Research Reviews 43 (2003) 110–133

11. https://nationalmaglab.org/education/magnet-academy/learn-the-basics/stories/mri-a-guided-tour

12. Bhargav Bhatt, M.Ramasubba Reddy, "Theoretical Analysis of Induced Potentials due to Blood Flow under the Static Magnetic Field of MRI". Indian Journal of Biomechanics: Special Issue (NCBM 7-8 March 2009)

13. Y. Kinouchi, H. Yarnaguchi, and T.S. Tenforde. "Theoretical Analysis of Magnetic Field Interactions with Aortic Blood Flow". J Bioelectromagnetics 1996; 17,21-32.

15. Valentina Hartwig 1, Giulio Giovannetti "Biological Effects and Safety in Magnetic Resonance Imaging: A Review" Int. J. Environ. Res. Public Health 2009, 6, 1778-1798; doi:10.3390/ijerph6061778

16. R. S. Popovic, Hall effect devices: Institute of Physics, 2004.

17. Charles Ellis, Microelectronics Fabrication and Design. Auburn University,2014

18. Wuyne R. Hudsogz, Erwi ~H . Meyu,and CZurence W . Schultx "TRANSISTOR PERFORMANCE IN INTENSE MAGNETIC FIELDS". NASA TN D-5428. September 1969

19. C. Possanzini1, and M. Boutelje1, "Influence of magnetic field on preamplifiers using GaAs FET technology"

20. Edward Daw, Richard F. Bradley "Effect of high magnetic fields on the noise temperature of a heterostructure field-effect transistor low-noise amplifier"

21. Guofu Niu, Semiconductor devise class note. Auburn University, 2013

22. Jasper HH, "Report of the Committee on Methods of Clinical Examination in Electroencephalography". Electroenceph. Clin. Neurophysiol. 10: 370-1.

24. B. 1. Roth. A. Pascual Leone. L. G. Cohen. M. Hallett. The heating of metal electrodes during rapid-rate magnetic stimulation: a possible safety hazard. Electroencephologr. Clin. Neurophysiol. 85, 116-123 (1992).

25. Koli, K., and Halonen, K.A.I.: "CMRR enhancement techniques for current-mode instrumentation amplifiers", IEEE Trans. Circuits Syst I,2000, 47, (5)

26. Franco, "Design with Operational Amplifiers and Analog Integrated Circuits", 3rd Edition, McGraw-Hill, 2002.

27. Charles Kitchin and Lew Counts, "A DESIGNER'S GUIDE TO INSTRUMENTATION AMPLIFIERS" 3RD Edition, Analog Devise.

28. P.R. Gray and R.G. Meyer, "MOS operational amplifier design – A tutorial overview," IEEE J.Solid – State Circuits, vol. SC-17, pp. 969 – 982,December 1982.

29. J.H. Nielsen and T. Lehmann, "An implantable CMOS amplifier for nerve signals." Analog Int. Circ. Signal Proc., vol. 36, pp. 153–164, July–Aug. 2003.

30. Jannik Hammel Nielson AND Erik Bruun," A CMOS Low-Noise Instrumentation Amplifier Using Chopper Modulation". Analog Integrated Circuits and Signal Processing, 42, 65–76, 2005